Master Degree in Electrical Engineering

Design of axial flux motors for automotive purpose

Relatore:
Prof. Michele Angelo Pastorelli

Autore:
Francesco La Greca

Supervisore Aziendale:
Ing. Fabrizio Impinna

A.Y. 2021/2022

Contents

Chapter 1

Introduction

1.1 Objective and Method

The objective of this work of thesis is to define a standardised procedure to fully design an electrical motor for automotive traction purpose with high performances in terms of acceleration and maximum achievable speed. The perfromance required leads to the necessity of an appropriate flux weakening (reaching high speed) and an appropriate power rating. The method used to reach the proposed goals is to fix the vehicle powertrain desired specifics, this allows to assign the power rating and the torque of the motor as starting points of the design (3.1). Once the motor is designed, a finit element analysis (**FEA**) is used to verify the results obtained.

1.2 Background Knowledge

In this section is reported a brief history of EV traction system and an analysis of the nowadays state of art.

1.2.1 History of the electric traction systems

The first electric car was designed and built in 1835, earlier than the IC propelled cars, the law autonomy of the batteries of that time were not a big issue since only big cities were paved. With the rise of oil consumption and the expansion of the modern road system (with inherent increasing autonomy demand) the internal combustion (IC) propelled car gained more and more space in the car industry totally overwhelming the electric vehicles. Electric vehicles returned to gain interest in the $60's$ with the developement of **power electronics** and later on with the oil crisis in the $70's$. Prototypes developed

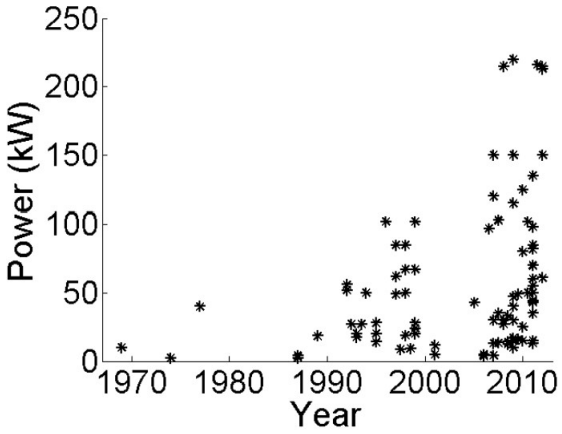

Figure 1.1: Power ranking of the EV's released on the market [15]

in this period set the basis of modern electric vehicles, however some issues prevented the EV to be predominant in the market: High prices and low power density of the batteries among others. Nowadays EVs have become attractive for the vehicle market thanks to a new socio-economic factors such as environmental issues and the will of many countries to gain independence from oil. Thanks to the new technological developments, such as NeFeB permanent magnets and better battery systems, is now possible to produce EV's with higher and higher power ratings as show in the figure 1.1.

1.2.2 State of art analysis

In the modern EV's traction systems, many different choices can be taken in terms of what motor to use. Here is reported a brief overview of the most common choices:

- **DC Motor** Before the development of the modern power electronics, this solution was widely used in variable speed applications due to the relatively easy control techniques. The torque-speed characteristic is quite good and a high constant torque is achievable. With the advent of power electronics the DC motor become obsolete due to many drawbacks such as high volume needed, low reliability, costly maintenance of the brushes.

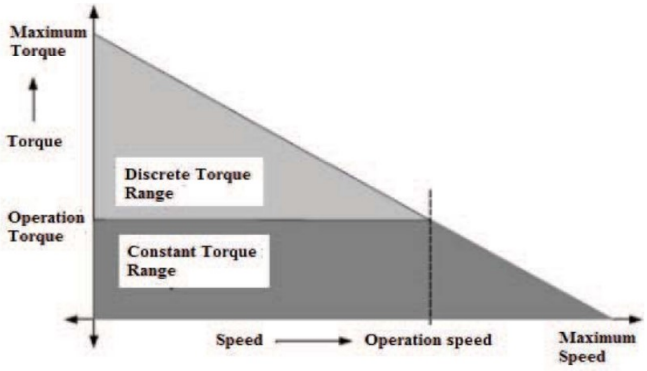

Figure 1.2: Torque characteristic for a DC motor [9]

- **Induction Motor** (**IM**) Induction motors are commonly used in EV applications because of the simple structure, reliability, robustness, easy maintenance, low cost and the capability of operating in poor environmental conditions. Induction motors have low efficiency if compared to PM motors due to the presence of currents in the rotor cage (or windings).

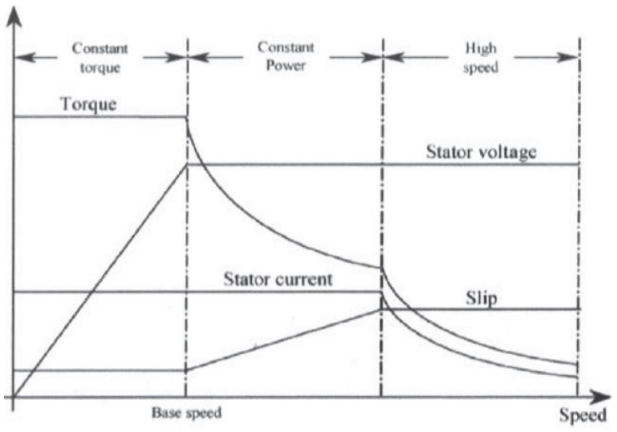

Figure 1.3: Torque characteristic for a Induction motor [9]

- **Permanent magnet brushless motor** (**PM**) Because of the presence of permanent magnets and the associated issues in having a proper flux weakening, the high speed region of the this kind of motors is limited. The costant power region can be extended varying the conduction angel of the current (flux weakening technique). This motors are highly sensitive to the temperature due to the demagnetizaiton issue.

Brushless motors can be found both for DC (BLDC) and AC (BLAC) applications, the main differance is in the supply EMF waveform.

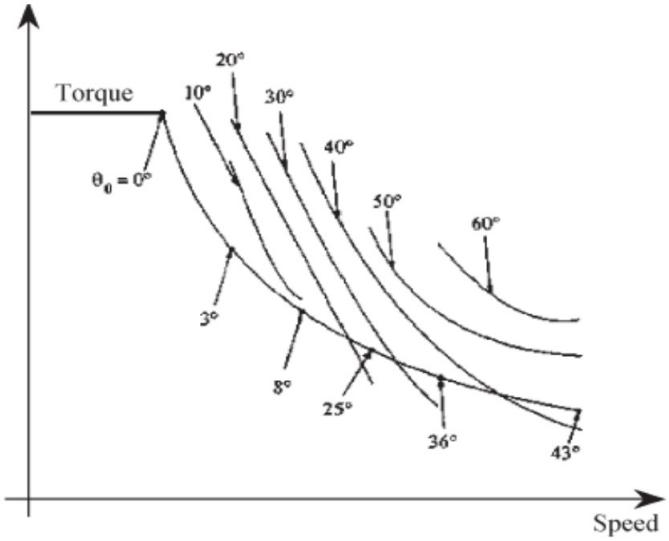

Figure 1.4: Torque characteristic for a BL motor at different conduction angle [9]

- **Switched reluctance motor** (**SRM**) This kind of motor takes advantage on the higly variable reluctance between the stator and the rotor at different angles. SRM has a large high speed region, it is fault tollerant and has high robustness. The major drowbacks are the high torque ripple and the noise due to mechanical vibrations.

Nowadays the DC motor solution is largely unused due to maintenace issues and low power density if compared to the AC solutions. Using an induction motor or a SRM is preferable when the application demands low production costs and a very high speed region. On the other hand, when an high efficiency and high power density are needed, the permanent magnet solution is the most suitable one. To achieve a larger high speed region is possible to use flux weakening technique combined with fractional slot tooth windings tecnology even if this solution has an impact on the overall efficiency due to higher harmonics distributions in the air gap (see 3.4.1). In the figure below is reported a brief summary of the main characteristics of the motors discussed in this section:

Characteristics		**Motor type**		
	DC	**IM**	**PM**	**SRM**
Power density	Low	Medium	Very high	Medium
Efficiency	Low	Medium	Very high	Medium
Controllability	Very high	Very high	High	Medium
Reliability	Medium	Very high	High	Very high
Technological maturity	Very high	Very high	High	High
Cost	Low	Very low	High	Low

Figure 1.5: EV motors main characteristics comparison

In table 1.1 is reported a survey made by the author about the most used traction solutions in the newest vehicles available on the market. The survey is necessary to understand how the EV's industry works and what aspects and characteristics are considered the most important ones.

As it can be seen there is a tendency in using Permanent Magnet motors (both AC brushless and DC brushless). Some important car manufacturers use IM instead of PM, this can be interpreted as the will to lower the costs or reaching high speeds easily. Even if the trand seams to be using radial flux motors type, axial flux motor are gaining interest in the EV industry thanks to some peculiar characteristcs. In the subsection 3.2.1 a deeper comparison of this two kind of motors is done. Nowadays the main reasons because axial flux motors are not so widely used is that the tachonlogy is not mature enoght and this means higher manufaturing cost and production time.

Vehicle Model (year)	**Brand**	**Motor**
e-trone 55 (2020)	Audi	IM
KONA electric (2019)	Hyundai	PM
Leaf SL Plus (2019)	Nissan	AC syncronous
CITIGOe iV (2020)	Skoda	PM
i3s (2020)	BMW	AC syncronous
I-Pace (2020)	Jaguar	PM
Corsa-e (2020)	Opel	AC syncronous
e-Nitro (2020)	Kia	PM
Model S (2022)	Tesla	IM
ID.4(2021)	Volkswagen	DC Brushless
XC40 (2021)	Volvo	PM
Taycan (2020)	Porsche	PM
500e (2019)	FIAT	PM

Table 1.1: Vehicle characteristics

Chapter 2

Background

2.1 Electromagnetism Principles

Every rotating electrical machine works thanks to the interaction of magnetic fields produced by excited windings and (or) permanent magnets, the mutual coupling of these fields produces torque with respect to the rotation centre of the machine (shaft). In this subsection are reported the main theories of electromagnetism that allows a better comprehension of the rotating electric machines functioning principles. The electromagnetic phenomena are well described by **Maxwell laws**. The main quantities involved in Maxwell equations are:

- Electric field strenght $\vec{E}$ $[V/m]$
- Magnetic field strenght $\vec{H}$ $[A/m]$
- Electric flux density $\vec{D}$ $[C/m^2]$
- Magnetic flux density $\vec{B}$ $[T]$
- Current density $\vec{J}$ $[A/m^2]$
- Electric charge density ρ $[C/m^3]$

The nature of an electromagnetic field can be deduced by the force vector that the field produces on a charge or a current carrying conductor according to the **Lorentz law**:

$$dF = dQ(\vec{E} + \vec{v} \times \vec{B}) = dQ\vec{E} + \frac{dQ}{dt}d\vec{l} \times \vec{B} = dQ\vec{E} + id\vec{l} \times \vec{B} \qquad (2.1)$$

The latter part of equation 2.1 describes the way in which the torque is produced inside an electrical rotating machine. A linear conductor, carrying

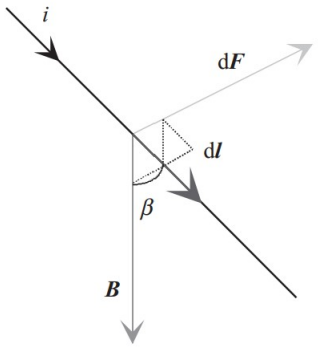

Figure 2.1: Graphical representation of Lorentz force [16]

a current i, with infinitesimal length $d\vec{l}$ crossed by a magnetic flux density filed $\vec{B}$ is subjected to an infinitesimal force $d\vec{F}$ whose direction is given by the vector product.

2.1.1 Maxwell laws: differential form

In order to give Maxwell equations independence from the shape of the area under observation or his position, they can be written as differential equations:

$$\nabla \times \vec{E} = -\frac{\partial \vec{B}}{\partial t} \tag{2.3}$$

$$\nabla \times \vec{H} = \vec{J} + \frac{\partial \vec{D}}{\partial t} \tag{2.4}$$

$$\nabla \cdot \vec{D} = \rho \tag{2.5}$$

$$\nabla \cdot \vec{B} = 0 \tag{2.6}$$

Equation 2.3 describes the ability of a magnetic flux varying in time to produce an electrical field around its field lines. Equation 2.4 describes the ability of a current varying in time to produce a magnetic field around its flowing direction and it's known as **Ampere's law**. Equation 2.5 is known as **Gauss law** and describes the tendency of an electric flux to flow always from a positive chearge to a negative one. Equation 2.6 describes the nature of the magnetic flux density field to be always circular with no ending or starting points.

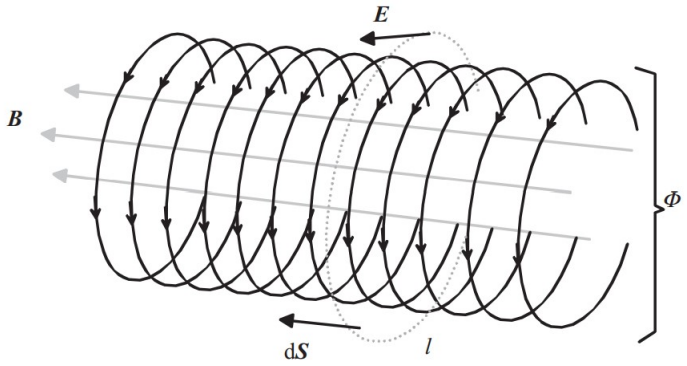

Figure 2.2: Graphical explanation of Faraday's induction law [16]

2.1.2 Maxwell laws: integral form

Maxwell equations lead to interesting considerations when reported in integral form:

$$\oint_l \vec{E} \cdot d\vec{l} = \frac{d}{dt} \iint_s \vec{B} \cdot d\vec{S} = -\frac{d\Phi}{dt} \tag{2.7}$$

$$\oint_l \vec{H} \cdot d\vec{l} = \iint_S \vec{J} \cdot d\vec{S} + \frac{d}{dt} \iint_S \vec{D} \cdot d\vec{S} = i(t) + \frac{d}{dt} \iint_S \vec{D} \cdot d\vec{S} \tag{2.8}$$

$$\oint_S \vec{D} \cdot d\vec{S} = \iiint_V \rho_v dV \tag{2.9}$$

$$\oint_S \vec{B} \cdot d\vec{S} = 0 \tag{2.10}$$

Equation 2.7 is known as **Faraday's induction law** and describes how a variation of the magnetic flux penetrating a surface described by the vector $\vec{S}$ is equal to the negative line integral of the electric field strength along the line l that identifies the surface contour (see fig.2.2). This equation is fundamental to calculate the voltage induced in the stator winding due to the rotor magnetic field, this voltage is called **back electro-motive force**, or **back-EMF**. In other words a short-circuited conductor wire crossed by a variable magnetic flux is subject to a voltage that produces a current. The current flowing in the wire induces a magnetic field opposite to the flux penetrating the surface that has the wire as contour. If the wire is wounded

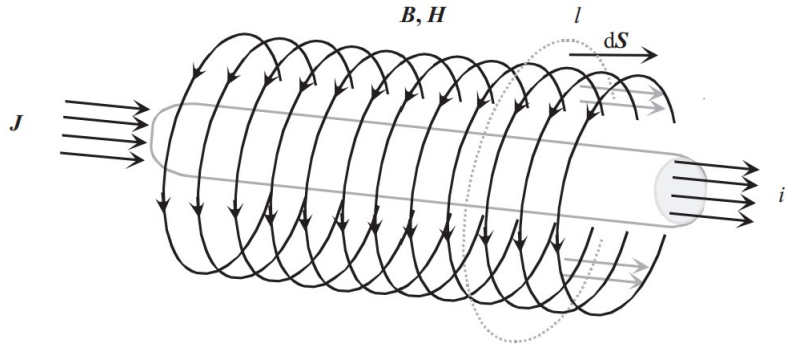

Figure 2.3: Graphical explanation of Ampere's law [16]

in order to form a coil of N turns and the flux does not penetrate all the turns completely but only a portion k_w of them, equation 2.7 become:

$$e = -k_w N \frac{d}{dt} \iint_S \vec{B} \cdot d\vec{S} = -k_w N \frac{d\Phi}{dt} = \frac{d\psi}{dt} \tag{2.11}$$

k_w is the so called **winding factor** and e is the **electro-motive force**, ψ is the **flux linkage**. The flux linkage can be expressed both as:

$$\psi = N k_w \Phi = LI \tag{2.12}$$

Where L is the **inductance** and represents the ability of a coil to produce flux linkage when a current crosses it and I is the RMS value of the current in the phase coil.

Equation 2.8 is well described in figure 2.3. When working with electrical rotating machines the range of frequencies employed allows to neglect the effects of $\vec{D}$ and the Ampere's law becomes:

$$\oint_l \vec{H} \cdot d\vec{l} = \iint_S \vec{J} \cdot d\vec{S} = \sum_{n=1}^{N} i_n(t) = \Theta(t) \tag{2.13}$$

Where Θ is the sum of the instantaneous values of the sum of the currents flowing in each of the N turns and is called **current linkage**

Equation 2.10 indicates that the sum of the magnetic flux through a close surface is zero, in other words does not exist a source for the magnetic field, this property is called **solenoidality**.

2.1.3 Numerical solution

Because of equation 2.10 it is always possible to express the magnetic field by the means of a **magnetic vector potential** $\vec{A}$.

$$\vec{B} = \nabla \times \vec{A} \tag{2.14}$$

To define the vector potential is also necessary to apply a gauge condition known as Coulomb's condition:

$$\nabla \cdot \vec{A} = 0 \tag{2.15}$$

The combination of equations 2.3 and 2.14 leads to:

$$\nabla \times \vec{E} = -\nabla \times \frac{\partial}{\partial t}\vec{A} \tag{2.16}$$

From equation 2.16 we deduce that electric strength field can be expressed as a function of $\vec{A}$ end ϕ which is the **electric scalar potential**.

Since $\nabla \times \nabla\phi = 0$:

$$\vec{E} = -\frac{\partial}{\partial t}\vec{A} - \nabla\phi \tag{2.17}$$

The equation shows that the electric field strength can be expressed as the sum of two contributes, a rotational part induced by the time dependence of the magnetic field, and a non-rotational part created by electric charges and the polarization of dielectric materials.

The current density is now expressed as:

$$\vec{J} = \sigma\vec{E} = -\sigma\frac{\partial}{\partial t}\vec{A} - \sigma\nabla\phi \tag{2.18}$$

From Amper's law and the definition of vector magnetic potential and known that $\vec{B} = \mu\vec{H}$:

$$\vec{J} = \nabla \times (\frac{1}{\mu} \times \vec{A}) \tag{2.19}$$

Combining equations 2.18 and 2.19:

$$\nabla \times (\frac{1}{\mu} \times \vec{A}) + \sigma\frac{\partial}{\partial t}\vec{A} + \sigma\nabla\phi = 0 \tag{2.20}$$

Equation 2.20 is valid in areas where eddy currents may be induced, whereas 2.19 is valid in areas with source currents $J = J_s$, such as winding currents, and areas without any current densities $J = 0$.

Chapter 3

Design

3.1 Chose of the requirements

The first step in electrical rotating machine design is to impose some motor requirements that help to reduce the wide range of possible initial choices (see also 3.3.1). The requirements are imposed by the designer, the motor has to satisfy them. In the case under exam the fixed requirements are:

- Nominal Power P_n $[kW]$
- Nominal Torque T_n $[Nm]$

Once the fixed requirements are identified, it is necessary to impose a design value for each one. A wise strategy to decide a proper value for the motor fixed requirements is to set, downstream, the application goals. In the case under exam the application environment is the powertrain of an electric vehicle and the goals are the vehicle specifics:

- Maximum Speed v_{max} $[km/h]$
- Maximum acceleration a_{max} $[m/s^2]$
- Maximum slope allowing the start

The full procedure that brings to the definition of the motor requirements is resumed in the following flow chart.

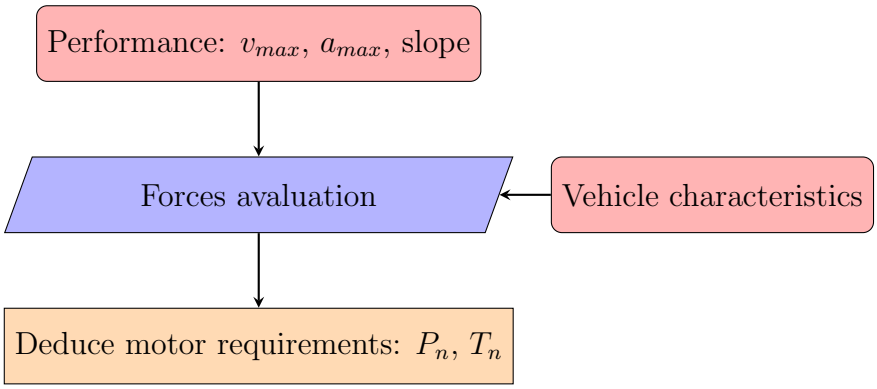

3.1.1 Vehicle characteristics

The vehicle chosen for the study has the characteristics reporterd in table 3.1 below.

Vehicle data	**Value**	**Symbol**
*Mass**	$1680kg$	m
Drag Coefficient	0.3	C_x
Surface	$2.44m^2$	s
Mass center height	$450mm$	h_g
Powertrain Data		
*Motor inertia**	$0.06kgm^2$	J_m
Transmission ratio	7	Tau
transmission efficiency	0.97	μ_t
Wheel data		
Width	$155mm$	W
Aspect ratio	0.7	AR
Tire diameter	$19inch$	D
Tire inertia	$0.6kgm^2$	J_w
Static friction coefficient	0.0084	f_0
Dynamic friction coefficient	$6.5 \cdot 10^{-6}$	k

Table 3.1: Vehicle characteristics

The data signed with "*" are given arbitrary since the motor has not been designed yet and they are deduced from similar projects. Starting from the vehicle characteristics it is possible to calculate the forces that need to be overcome by the traction system during the linear uniform motion of the vehicle, this will be better explained in the next subsection.

3.1.2 Driving forces evaluation

In this subsection an analytical evaluation of the resisting force acting on the vehicle during his motion is proposed. The main forces that contribute to the mechanical balance are graphically reported in fig.3.1 below.

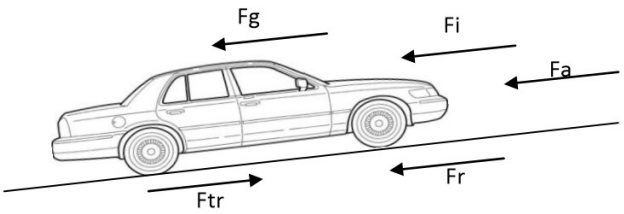

Figure 3.1: Vehicle forces

where:

- **Traction Force**

$$F_{tr} = \mu_t \cdot \frac{T}{Tau} \cdot \frac{D}{2} \tag{3.1}$$

  Where T is the torque produced by the motor.

- **Parallel component of gravitational force**

$$F_g = m \cdot g \cdot sin(\Theta) \tag{3.2}$$

  Where Θ is the road slope angle and g is the gravitational acceleration constant.

- **Inertial resistance force**

$$F_i = m_{eq} \cdot acc \tag{3.3}$$

  Where

$$m_{eq} = m + 4J_w/R_e^2 + J_m tau^2/R_e^2 \tag{3.4}$$

  R_e is the effective rolling radius of the tire evaluable as the ratio between the vehicle speed v and the tire angular speed ω.

- **Aerodinamic drag resistance**

$$F_a = \frac{1}{2} \cdot \rho \cdot C_x \cdot v^2 \tag{3.5}$$

  Where ρ is the air density.

- **Rolling resistant force**

$$F_r = m \cdot g \cdot cos(\Theta)[f_0 + kv^2] \tag{3.6}$$

The driving resistant force has to be balanced by the traction system to move the vehicle with uniform straight motion and has to be overcome to produce the vehicle acceleration. The driving resistant force with and without slope is reported, in function of the vehicle speed in fig.3.2

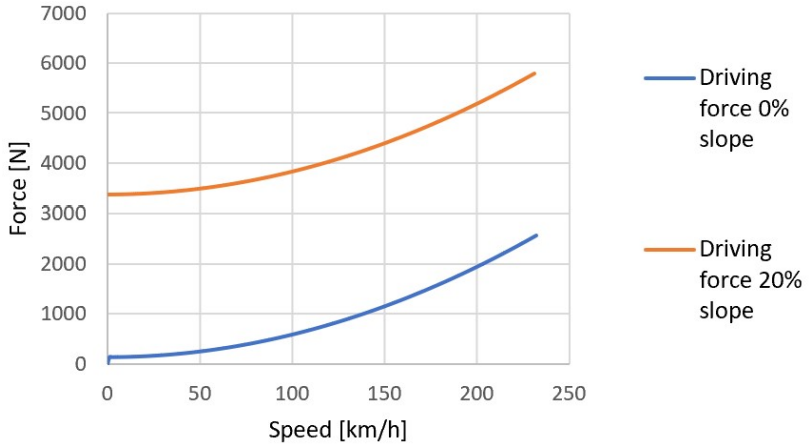

Figure 3.2: Driving resistent force

The figure shows how the resistant force tends to increase with the speed.

3.1.3 Assign the motor requirements: Power

The power needed to move the vehicle boils down to the following equation:

$$P = (F_g + F_i + F_a + F_r)v + m_{eq}\frac{dv}{dt}v = F_{res} \cdot v + \frac{m_{eq}}{a} \cdot v \tag{3.7}$$

This equation allows to deduce the nominal power P_n needed to move the vehicle up to the maximum speed desired v_{max}. It is worth noting that in case of rectilinear and uniform motion the second addend of the second term of the equation has to be set equal to zero in order to give mathematical consistency.

The static speed to power characteristic is reported in fig.3.3

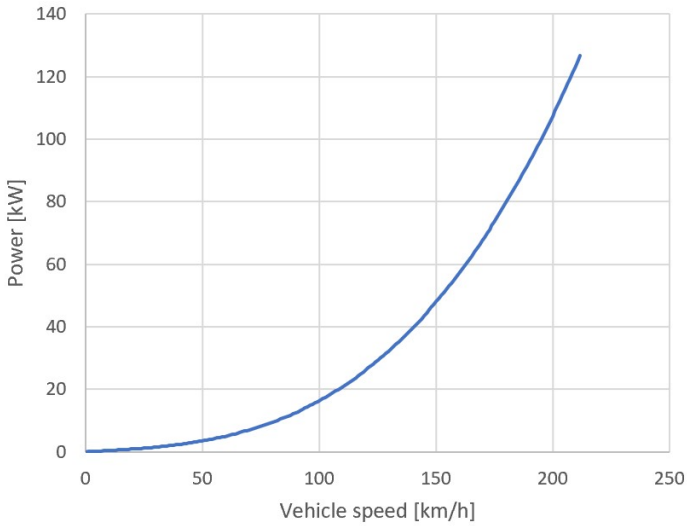

Figure 3.3: Power needed to move the vehicle in uniform motion

It is deduced that a power of $130kW$ is required to move the vehicle up to $210km/h$ which is the v_{max} specific.

3.1.4 Assign the motor requirements: Torque

In order to satisfy the specific of maximum acceleration a_{max} is necessary to produce a certain torque at the wheel that corresponds to a driving force.

$$F_{wheel} = m_{eq} \cdot a_{max} + F_{res}(v) \tag{3.8}$$

$$T_{wheel} = F_{wheel} \cdot R_e \tag{3.9}$$

$$T_{motor} = \frac{T_{wheel}}{Tau} \tag{3.10}$$

So that the force needed at the wheel is equal to the sum of the total resistant force, which is a function of the speed, and the product between the maximum acceleration required by the specifics and the equivalent vehicle mass that takes into account the presence of moving rotating masses in the power train. Once the moving force needed has been calculated, the torque at the wheel and at the motor is immediately deducible.

The torque chosen to guarantee the acceleration specific has to be high enough to allow the vehicle to start in slope conditions. At the end of the analysis a torque of $350Nm$ has been chosen. In fig.3.4 is reported the motor torque characteristic.

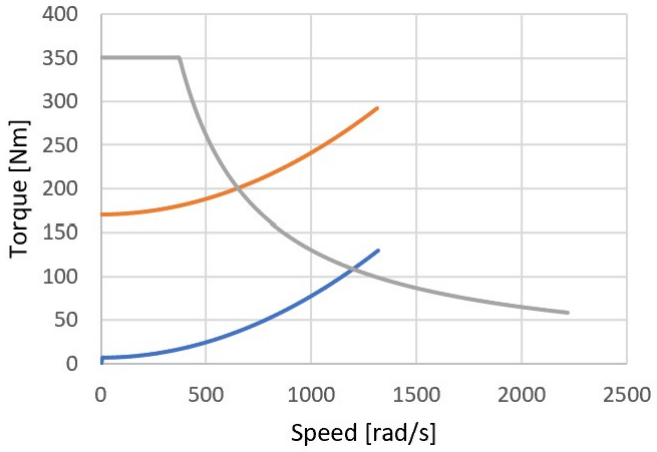

Figure 3.4: Motor torque characteristic

With this torque-speed characteristic, the speed profile is as shown in figure 3.5.

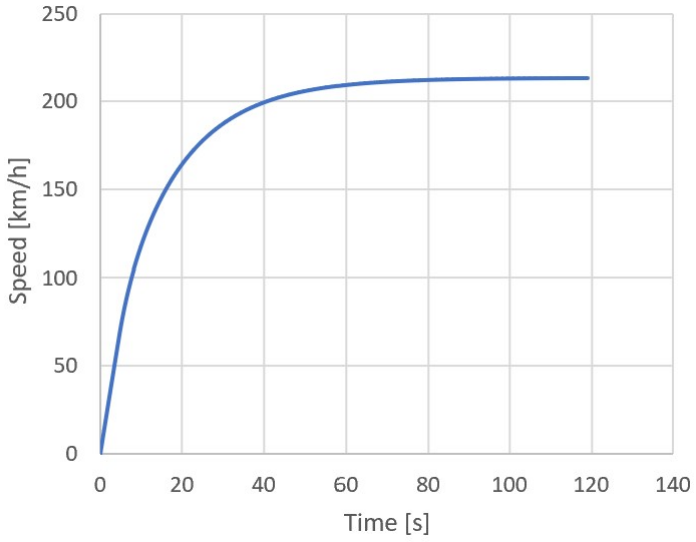

Figure 3.5: Vehicle speed applying the maximum torque available

The results obtained after the requirements assignment study are reported

in table 3.2.

Vehicle Specific	**Value**	**Symbol**
Maximum velocity	$210[km/h]$	v_{max}
Maximum acceleration	$0-100[km/h]$ in $8[s]$	a_{max}
Maximum slope	20%	Θ
Motor Requirements		
Nominal Power	$130[kW]$	P_n
Nominal Torque	$350[Nm]$	T_n
Supply Circuit Requirements		
DC-link voltage	$400[V]$	V_{dc}

Table 3.2: Vehicle and motor fixed specifics

The choice of a $400V$ DC-link has been done for industrial standardization reasons.

3.2 Choosing the motor type

Once the motor requirements have been set, it is necessary to decide what kind of motor can suit the application the most. Since the application requires a great power density and high efficiency, the permanent magnet motors are the best choice as seen in 1.2.2. There are several types of permanent magnet motors, they can be included in two macro-groups:

- **Radial flux motor(RFM)**

  Has the typical layout shown in figure 3.6. The permanent magnets are positioned on a cylindrical rotor (the rotor can be exterior as well) and magnetized radially with respect to the rotation centre point (shaft). The wide knowledge about this technology has lead to a great spread in the most common industrial applications. Nowadays radial flux motors are relatively easy to produce in large scale with a positive impact on the manufacturing costs.

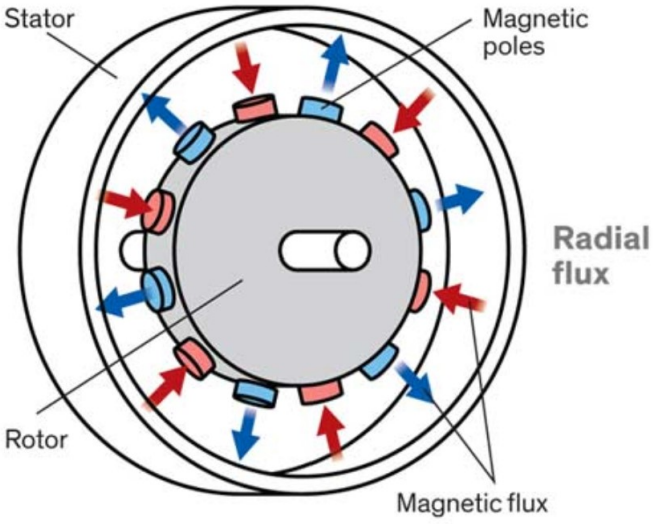

Figure 3.6: Typical radial flux machine layout

- **Axial flux motor(AFM)**:

  Has the typical layout shown in figure 3.7. The permanent magnets are positioned on a circumference equally spaced from the rotation centre (shaft). The magnets are magnetized axially with respect to the rotor circumference. This kind of motor is the first ever existed, despite this the non trivial manufacturing procedures prevent them to be used in the most common industrial applications. Nonetheless thanks to the recent technological progress, the use of new material and a deeper knowledge, some manufacturers are now beginning to produce this kind of motors.

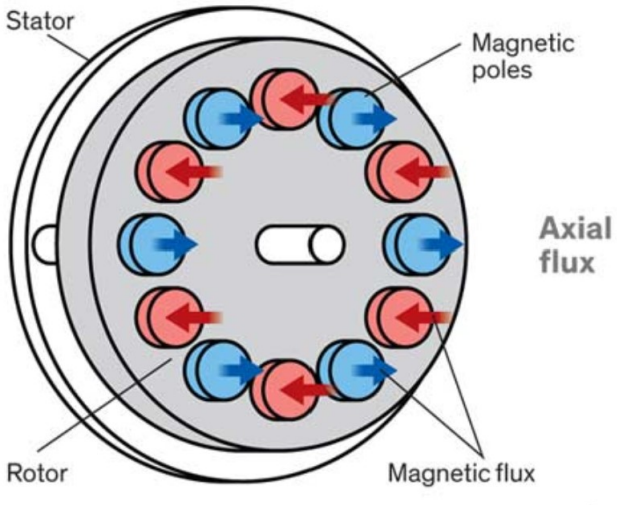

Figure 3.7: Typical axial flux machine layout

One big advantage of AFM is the possibility to use more than one stator or more than one rotor in order to increase the number of active air-gaps, this means more torque available at the shaft. Of particular interest are the **double stator** (**DSAFM**) and the **double rotor** (**DRAFM)** configuartions.

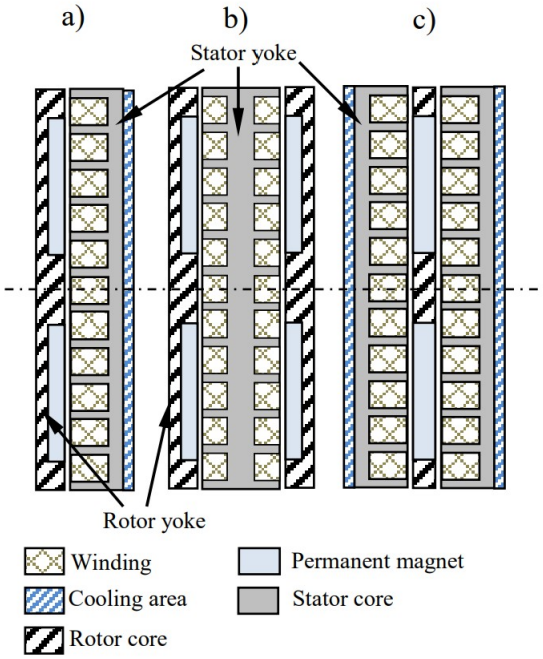

Figure 3.8: Axial flux permanent magnet motor: Single ai rgap, double rotor, double stator typology [14]

It is reasonable to prefer the double stator configuration instead of the the double rotor one, as a matter of fact the DSAFM prevents the axial attraction force between the stator and the rotor and allows an easier cooling.

The intimacy between stators windings and rotor magnets leads to the possibility to use non -magnetic materials for the rotor with many benefits in terms of material weight and inertia.

3.2.1 AFM versus RFM configuration

In this subsection the RFM and the AFM performances are analyzed together to deduce what typology best fits the request of the project.

It is well known that the output torque of AFM is way bigger than the RFM one, if the main dimensions are kept the same for both the configurations (see fig.3.9). The torque in an AFM goes with the power of three of the outer active diameter, in RMF the torque goes with the power of two of the active outer radius as shown in figure 3.10.

$$T_r \propto \frac{D_a^2 \pi L}{2} \tag{2.22}$$

$$T_{ax} \propto \frac{D_a^3 - D_i^3}{8} \frac{4\pi}{3} \tag{2.23}$$

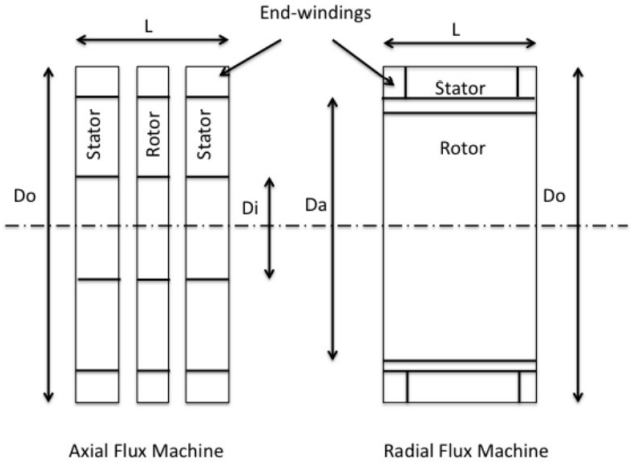

Figure 3.9: Scheme of axial and radial flux motor main dimensions [14]

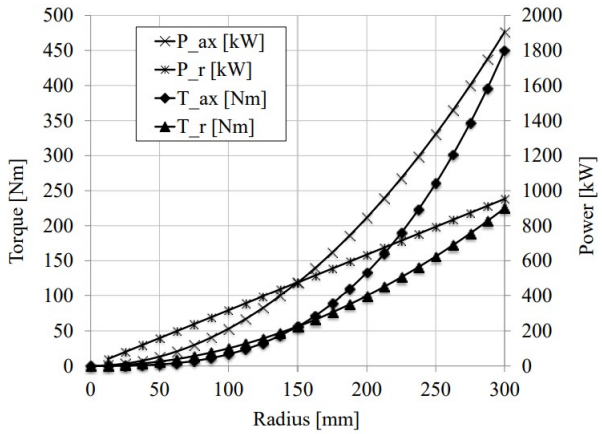

Figure 3.10: Axial and Radial flux motor torque and power comparison in function of the active radius $D_a/2$ [14]

From picture 3.10 it can be deduced that from a certain tradeoff point on the AFM is way more competitive, in terms of torque production, when compared to the RFM. Despite what has been said it is necessary to confront the two typology from other points of view.

The further comparative analysis is made between different kinds of RFMs and AFMs at different power ratings: $0,25kW$, $1kW$, $3kW$, $5kW$ and $10kW$.

The motor types under analysis are: Radial flux motor with inner rotor, Axial flux motor single gap, Axial flux motor dual gap, Axial flux motor single gap slotless, Axial flux motor dual gap slotless.

To perform an accurate analysis, some aspects have been kept in consideration:

1. For the slotless machines in each case except for the two smallest machines, the magnet thickness needs to be increased in order to overcome the higher reluctance due to the larger air gap created to accommodate the windings

2. The cross section of the copper wire is increased with the power output to reduce copper losses, this is generally a good practice to adopt when a design in scale procedure is used.

3. The airgap flux density is nearly the same for all of the slotted types but falls sharply for the slotless designs due to the large air gap despite the increasing magnet thickness.

4. The dual-gap axial field motor has a higher airgap flux density than the single-gap one because of the smaller air gap per side. In this case, the turns required per slot pitch are almost halved.

- **Volume comparison**

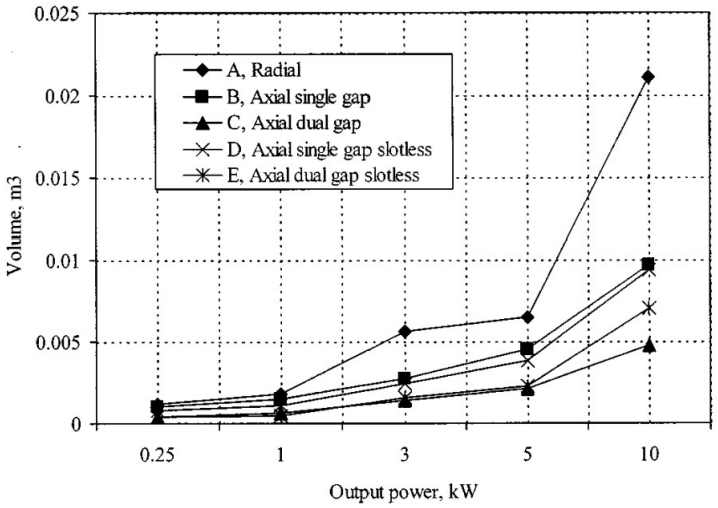

Figure 3.11: Active volume needed versus output power required[1]

Figure 3.11 shows the active volume required for a certain power output. With "Active volume" here is meant the total volume of stator teeth, stator back-iron, rotor back-iron and copper. For the RFM the volume needed is the largest one, this is due to the larger axial dimension with respect to the AFM. Any typology of AFM is more convenient than a RMF configuration when low active volume is required, even though the slottles typology requires more turns since the absence of an iron core in the stator.

- **Moment of inertia**

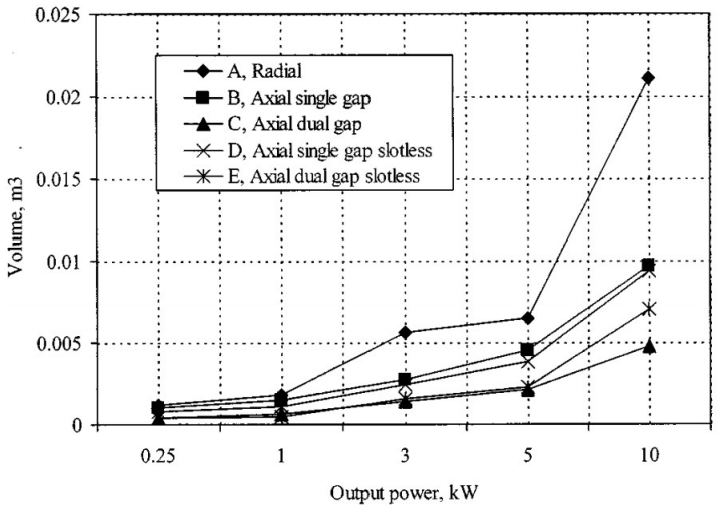

Figure 3.12: Moment of inertia versus output power required[1]

The RFM has the largest moment of inertia at any output power, this can be associated with a consequence of the higher active volume in particular with the bigger rotor length required. As a matter of fact the torque, in RFM, is produced at a fixed air gap diameter which is effectively smaller than the axial field motor where the torque-producing diameter grows radially for a fixed airgap length. It is worth noting that the dual-gap slotless machine has the lowest moment of inertia as it does not contain any steel in the rotor. In conclusion, when an high dynamic performance is required, the AFM is the best choice.

- **Steel weight**

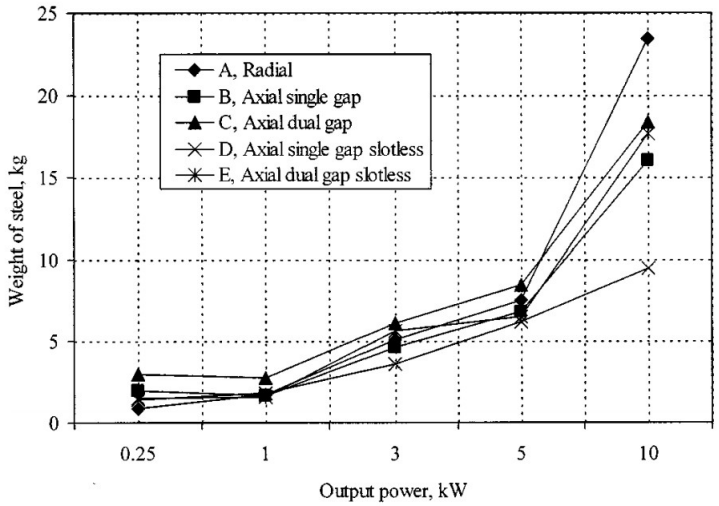

Figure 3.13: Weight of electrical steel needed versus output power required[1]

Since the single-gap slotless motor does not have any teeth, it requires less steel. Figure 3.13 shows that as the power rating increases, the slotless machines always require less iron than the radial flux machines. Intuitively, it may be seen that as the active volume of the motor gets higher, the weight also increases (see also figure 3.11).

- **Copper weight**

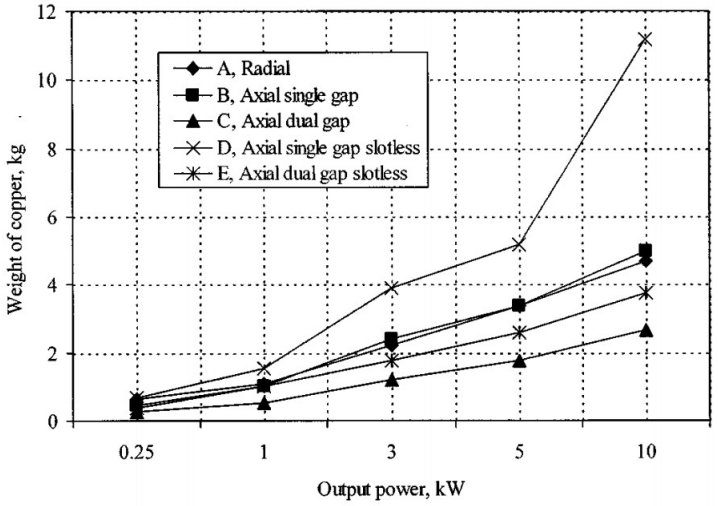

Figure 3.14: Weight of copper needed versus output power required[1]

The copper required by the radial flux and single-gap axial flux slotted machines is almost identical. Due to the low flux density in the airgap, the slotless single stator motor needs the biggest amount of copper to guarantee a certain power output. The double ai rgap axial flux motor requires less copper than the radial flux machine due to the presence of a larger magnet area moreover the stator teeth help to guide the flux through the stator and this results in a better exploitation of the air gaps. It is worth do be noticed that having more copper means more copper losses (see figure 3.16).

- **Magnet weight**

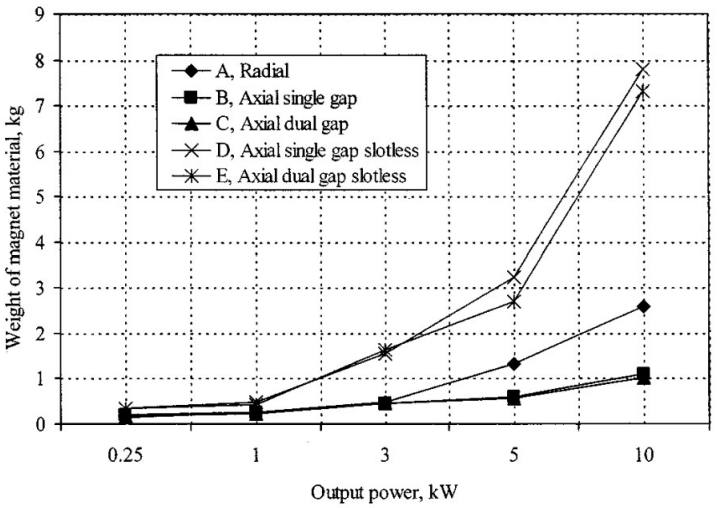

Figure 3.15: Weight of permanent magnet needed versus output power required[1]

The slotless motors need more magnets because of the large airgaps. The axial slotted motors need less magnets compared with the radial typology for every power rating analyzed, this is due to the larger active area available.

- **Copper losses**

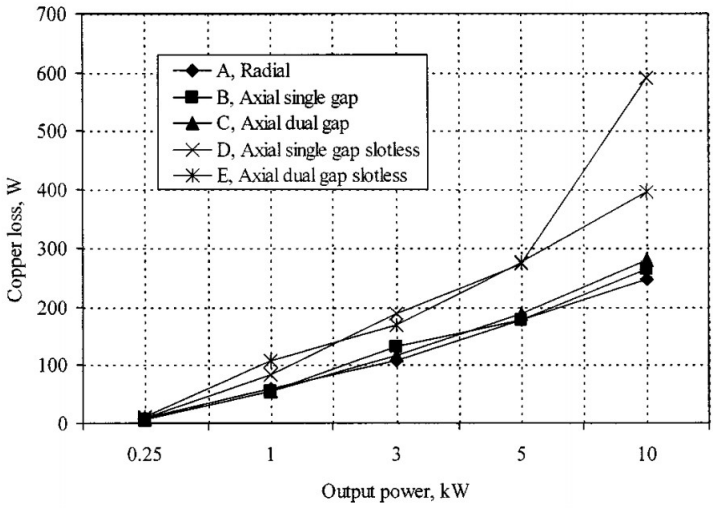

Figure 3.16: Joule losses versus output power required[1]

The current required by each of the machines at each of the power ratings is the same and losses are directly proportional to the copper weight. Higher copper losses means more sophisticated cooling systems. Beside it has to be considered that axial flux motor cooling is not trivial due to the intimacy between the stator and the rotor. When an high power ratio is required, the use of slotless motors might lead to overheating issues.

- **Iron losses**

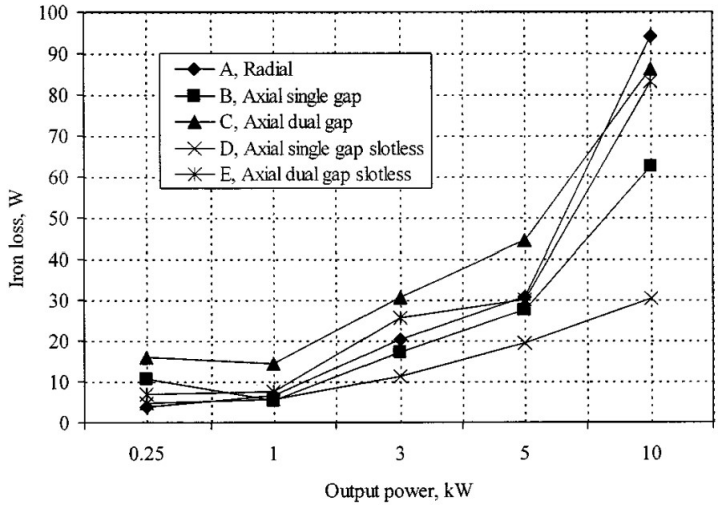

Figure 3.17: Iron losses versus output power required[1]

Similar to what already said for the copper losses, iron losses are proportional to the iron weight required in the machine.

For what has been said, the **double-gap axial flux slotted** machine is considered the best choice to suit the problem because of its higher torque production, low material volume needed (lower inertia) and higher overall efficiency.

3.3 Main Dimensioning

In this section all the procedures used to define the main dimensions of the double-gap axial flux slotted motor are reported.

3.3.1 Material Loading

The material loading, **linear current density** $A[A/m]$ and **magnetic flux density in the air gap** $B_g[T]$, have to be chosen arbitrarily at the beginning of the design procedure following past experiences or similar projects. In an axial flux PM motor the peak linear current density is a function of the radius as in the formula below.

$$A_m(r) = \frac{m \cdot \sqrt{2} I_a \cdot N_1}{\pi r} \tag{3.11}$$

In this work of thesis, when not specified, the value of linear current density is referred to the average radius $r = (r_{out} + r_{in})/2$.

The choice of material loading values influences deeply the final outcome of the project but they have to be chosen arbitrarily, as said, so the author decided to use an iterative approach (sec3.3.6): at first the material loading values have been chosen following indications found in literature [3] , once the dimensioning is finished the torque and back emf produced by the designed motor are evaluated and compared to the starting project value, the error between them needs to be less than a certain ε imposed downstream, the right values of A and B_g are the ones that satisfy this condition. As shown later in 3.3.3 another value that needs to be chosen arbitrarily is the ratio between the Back emf produced by the motor at the base speed with no load, E_f and the phase voltage V_1

$$\epsilon = \frac{E_f}{V_1} \tag{3.12}$$

This new term has to be added to the iterative procedure as well in order to obtain a choerent result.

3.3.2 Torque production

For a double stator PM axial flux machine is possible to express the electromagnetic torque produced as a function of the material loading starting from Lorentz's low introduced in 2.1:

$$d\overrightarrow{F_x} = I_a(\overrightarrow{dr} \times \overrightarrow{B_g}) = A(r)(d\overrightarrow{S} \times \overrightarrow{B_g}) \tag{3.13}$$

with $dS = 2\pi r dr$

$$T = 2\pi r_{in} \cdot A_{in} \cdot B_{max} \cdot r dr \tag{3.14}$$

and integrating with respect to the active region:

$$T = 2\pi B_{max} \cdot A_{in} \int_{r_{in}}^{r_{out}} r_{in} dr = 2\pi B_{max} v \cdot A_{in} \cdot r_{out}^3 k_d (1 - k_d^2) \tag{3.15}$$

$k_d = \frac{r_{in}}{r_{out}}$ is the ratio between the two main dimensions of the machine.

Deriving the equation with respect to k_D shows that the value that maximizes the torque is $k_d = 1/\sqrt{3}$ however this value is to be considered only as theoretical. The experience of many manufacturers and machine designers reported in literature shows how this value does not allow a proper construction of the machine because of the narrow space between the end connection in the interior part between the stator and the shaft. A value between 0.6 and 0.7 has to be chosen. The author chosed $k_d = 0.65$.

3.3.3 Sizing equations

The main dimensions of a double-sided PM brushless motor with internal disc rotor can be determined using the following assumptions:

- The electrical and magnetic loadings (A and B_g) are assigned.

- The number of turns per phase per one stator is N_1
- The phase armature current (maximum value) in one stator winding is I_a
- the back EMF per phase per one stator winding (maximum value) is E_f

Referring equation 3.11 to the main diameter of the machine brings to:

$$A_m = \frac{4\sqrt{2}m \cdot I_a \cdot N_1}{\pi D_{out}(1+k_d)} \tag{3.16}$$

The back EMF induced in one stator by the permanent magnets can be expressed as:

$$E_f = \pi\sqrt{2} \cdot n_s \cdot p \cdot N_1 \cdot k_{w1} \cdot \Phi_f = k_E \cdot n_s \tag{3.17}$$

thus, according to 3.16 and 3.17 , the apparent power for one phase considering both stators connected in series is:

$$S = m \cdot (2E_f) \cdot I_a = \frac{\pi^2}{8} \cdot k_{w1} \cdot n_s \cdot B_{mg} \cdot A_m \cdot D_{out}^3(1+k_d)(1-k_d^2) \tag{3.18}$$

for a better layout of the equation is possible to define:

$$k_D = \frac{1}{8}(1+k_d)(1-k_d^2) \tag{3.19}$$

$$S = \pi^2 k_D \cdot k_{w1} \cdot n_s \cdot B_{mg} \cdot A_m \cdot D_{out}^3 \tag{3.20}$$

alternatively the expression of the electromagnetic apparent power is:

$$S = \frac{\epsilon P_{out}}{\eta cos\varphi} \tag{3.21}$$

According to both 3.20 and 3.21 , the outer diameter is:

$$D_{out} = \sqrt[3]{\frac{\epsilon P_{out}}{\pi^2 k_D k_{w1} n_s B_{mg} A_m \eta cos\varphi}} \tag{3.22}$$

It is worth noting that in order to evaluate the outer diameter of the machine is not necessary to know the value of back EMF produced nore the phase current.

3.3.4 Magnetic flux

Now that the main active dimensions of the motor are defined it is possible to evaluate the magnetic flux inside the air gap. Assuming a sinusoidal distribution of the PMs magnetic flux density waveform, the average magnetic flux density is given integrating the peak flux density value with respect to the pole pitch:

$$B_{avg} = \frac{p}{\pi} \int_0^{\frac{\pi}{p}} B_{mg} sin(p\alpha) d\alpha = \frac{2}{\pi} B_{mg} \tag{3.23}$$

if the waveform is not sinusoidal the relationship become:

$$B_{avg} = \alpha_i B_{mg} \tag{3.24}$$

where α_i is the pole width to pole pitch ratio. The average magnetic flux inside the gap is now evaluable as:

$$\Phi_f = \int_{r_{in}}^{r_{out}} \alpha_i B_{mg} \frac{2\pi}{2p} r dr = \alpha_i B_{mg} \frac{\pi}{2p} (r_{out}^2 - r_{in}^2) \tag{3.25}$$

3.3.5 Number of windings per phase

The number of windings per phase per stator must be coherent with the linear current density, the air gap magnetic flux density and the voltage ratio (3.12) chosen at the beginning of the design process (see sec.3.3.1). Here are shown two different approaches to evaluate the number of windings based on each material loading, the final value obtained with both procedures must be similar to achieve an optimal design. If the two results are slightly different it is reasonable to accept an average value.

- **Linear current density based mathod**

  The linear current density 3.11 depends on the conductor geometry inside the machine and represents the way the current is distributed along a circumference of radius $r_{in} < r < r_{out}$. It is possible to consider only the circumference correspondig to the average radius without commit relevant mistakes. The number of windings per phase per stator necessary to guarantee the linear current density desired in the machine along the average radius is expressed as:

$$N_1 = \frac{\pi D_{out} (1 + k_d) A_m}{4 m \sqrt{2} I_a} \tag{3.26}$$

with

$$I_a = \frac{P_{out}}{m\sqrt{2}(2V_1)\eta cos\varphi} \tag{3.27}$$

where the value $2V_1$ is equal to the rms voltage value at the inverter output which is, in case of stator connected in series, two times the voltage applied to a single stator V_1.

- **Air gap magnet flux density based method** Once the flux density desired in the air gap is fixed, the back EMF produced must satisfy the voltage ratio ϵ chosen for the dimensioning (3.3.3), to do so a proper flux linkage must be produced and thus a proper number of winding per phase per stator must be chosen.

$$N_1 = \frac{\epsilon V_1}{\pi\sqrt{2} f k_{w1} \Phi_f} \tag{3.28}$$

with f frequency at the base speed.

Besides, a solution with concentrated windings (windings wounded around each single tooth) has been chosen. For an overview about this thecnology see 3.4.1.

3.3.6 The iterative procedure

Once the main dimension of the machine, the number of poles and slots (see 3.5) and the number of turns are chosen it is necessary to verify that the new machine satisfies the input parameters fixed at the beginning of the design procedure in table 3.2. If the motor produces different values of torque or back emf than the ones fixed, the material loadings A, B_g and the ratio ϵ must be changed until a match occurs.

To evaluate the torque and the back EMF produced it is necessary to calculate the torque and emf constants:

- **Torque constant** K_t

  According to equations 3.14 and 3.16, the torque produced by a double stator axial flux machine can be expressed as:

$$dT = 2\alpha_i m I_a N_1 k_{w1} B_{mg} r dr \tag{3.29}$$

  Integrating along the active length of the machine:

$$T = \frac{1}{4}\alpha_i m I_a N_1 k_{w1} B_{mg} D_{out}^2 (1 - k_d^2) \tag{3.30}$$

including equation 3.11 in the previous equation, the rms value of the torque become:

$$T = \frac{m}{\sqrt{2}} p N_1 k_{w1} \Phi I_a = K_t I_a \tag{3.30}$$

Finally the torque constant is:

$$K_t = \frac{m}{\sqrt{2}} p N_1 k_{w1} \Phi \tag{3.31}$$

- **EMF constant** K_{emf}

  The emf induced in one phase of the motor can be expressed starting from the first harmonic of the magnetic flux waveform as:

$$e_f = N_1 K_{w1} \frac{d\Phi_1}{dt} = 2\pi f N_1 K_{w1} \Phi cos(\omega t) \tag{3.32}$$

  The rms value is evaluable starting from the maximum value as follow:

$$E_f = \pi\sqrt{2} f N_1 K_{w1} \Phi = \pi\sqrt{2} p N_1 K_{w1} \Phi n_s = K_{emf} n_s \tag{3.33}$$

  Finally the back emf constant is:

$$K_{emf} = \pi\sqrt{2} p N_1 K_{w1} \Phi \tag{3.34}$$

Now that the machine constants and the main dimensions are defined, is possible to calculate the error between the torque and the EMF produced by the designed machine and the initial fixed values.

The chart below summarizes the main procedure for a proper iterative design process.

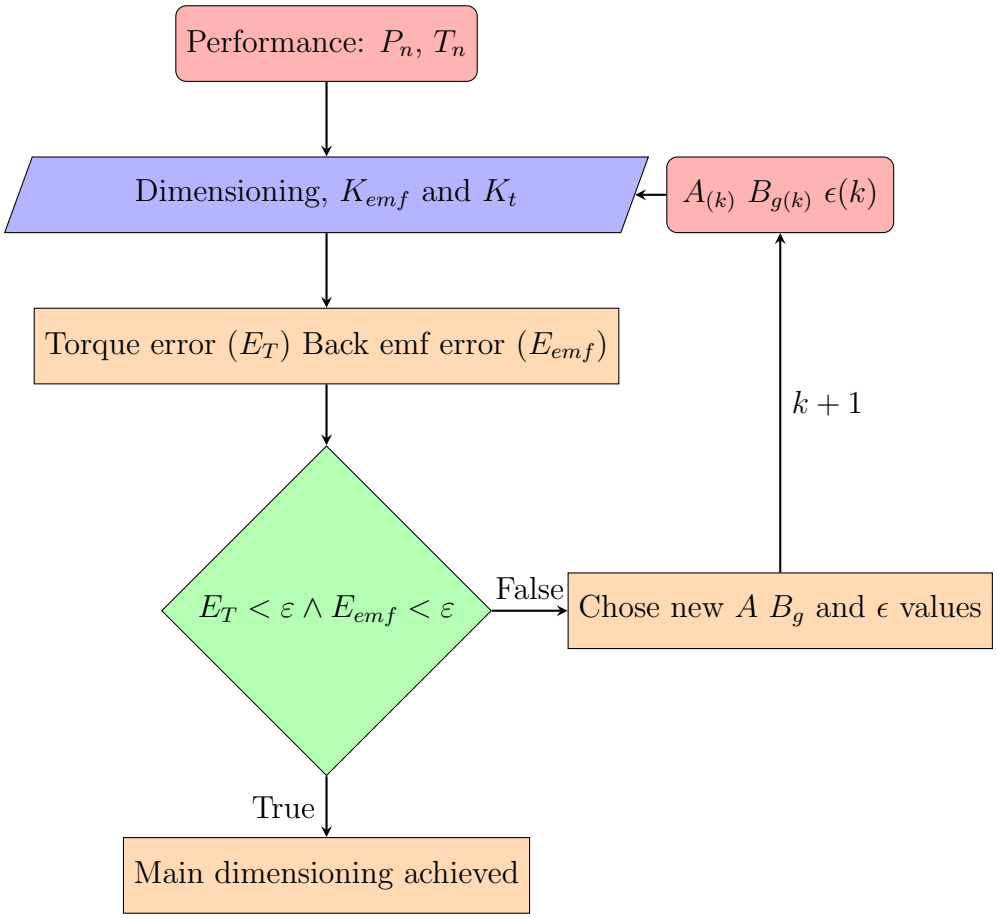

3.4 Winding Technology

One of the major aim of the motor project is to achieve a wide constant power working region, in order to do so the magnetic flux has to be easily reduced by the flux weakening technique. The ratio between the permanent magnet flux linkage and the synchronous inductance represents the **short circuit current** I_{ch}.

$$I_{ch} = \frac{\Psi_{PM}}{L_s} \tag{3.35}$$

Electrical machines with concentrated windings are well known to present higher values of inductance (if compared to similar machines with distributed windings) thanks to the higher harmonic components in the magneto-motive force produced. The phenomenon introduced above is treated in the following subsection.

3.4.1 Concentrated windings

The synchronous inductance of the machine is the sum of two components:

$$L_s = L_m + L_\sigma \tag{3.36}$$

where L_m is the **magnetizing inductance** and L_σ is the **leakage inductance**, the latter is typically negligible in common distributed windings machines while is the predominant one when concentrated windings are used. The leakage inductance in non-skewed machines can be calculated as follows:

$$L_\sigma = L_{ew} + L_u + L_d + L_\delta \tag{3.37}$$

with:

- L_{ew} end winding leakage inductance
- L_u slot leakage inductance
- L_d tooth tip leakage inductance
- L_δ air gap leakage inductance

The first three parameters are typically low and they are deeply influenced by the machine main dimensions and the number of conductors used. It is convenient to refer to this first three parameters as **constructional leakage inductance**.

$$L_{\sigma c} = L_{ew} + L_u + L_d \tag{3.38}$$

The **air gap leakage inductance** L_δ is due to the harmonic components of the magneto motive force resulting from the geometric nature of the windings and it is proportional to the magnetizing inductance. The ratio between L_m and L_δ is fixed for a certain pole/slot configuration despite the mechanical parameters, therefore:

$$L_\delta = L_m \cdot \sigma_\delta \tag{3.39}$$

Where σ_δ is the **harmonic leakage factor**. Taking as an example a configuration 18 slots and 16 pole as showned in figure 3.18

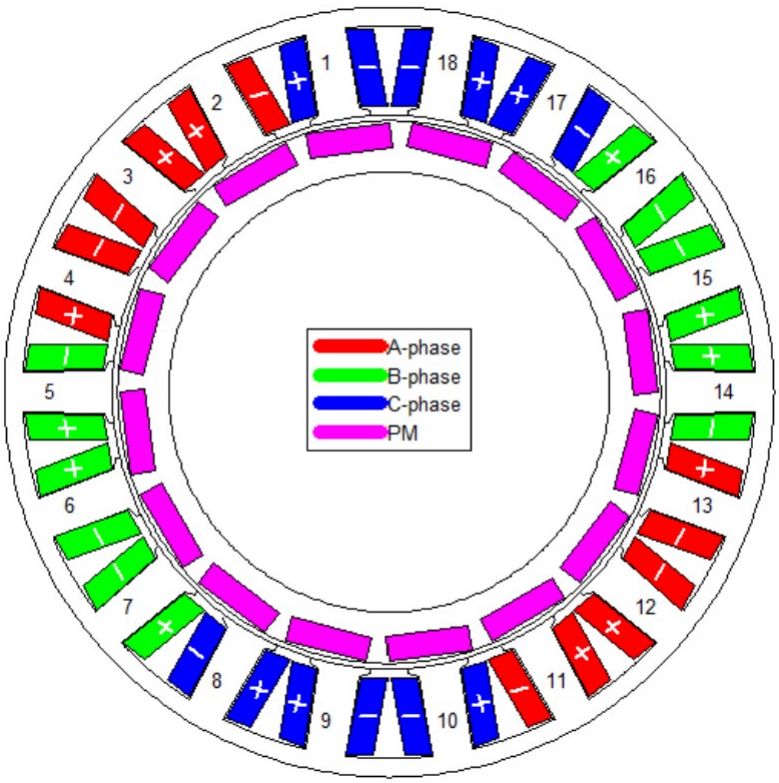

Figure 3.18: Motor layout 18 slots 16 poles [5]

The normalized current linkage $\Theta(\alpha)$, in Ampere-turns, generated by a single coil motor phase with $1A$ current is reported in 3.19 below.

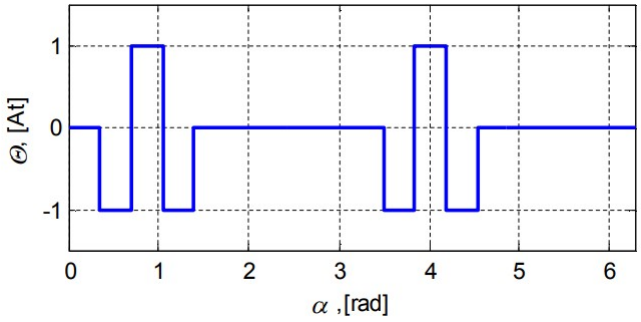

Figure 3.19: Winding function of a 18/16 machine [5]

To achieve an intuitive mathematical analysis of the winding function is necessary to introduce the **base winding approach**. Referring to the machine with his slot-pole ratio, for example $\frac{18}{16}$, the base winding is the one

described by a second ratio obtained by simplifying the first ratio ($\frac{18}{16}$) so that the numerator is the smallest number divisible by three and the denominator is the smallest number divisible by two. In this example the base winding ratio is $\frac{9}{8}$. Therefore it can be said that the $\frac{18}{16}$ machine is formed by two base $\frac{9}{8}$ machines with p_b pole pairs. In the case under exam $P_b = 4$.

The **current linkage harmonics** are deducible from the winding function as follow:

$$h = abs(\frac{FFT(\Theta(\alpha))}{n}) \tag{3.40}$$

where n is the number of samples of the winding function. The harmonic spectrum of the winding factor under exam is reported in 3.20.

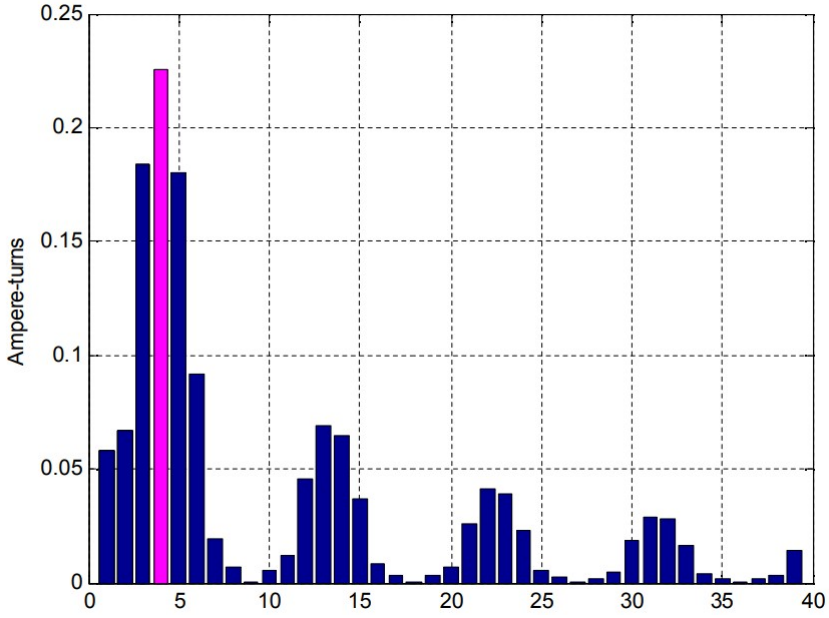

Figure 3.20: Winding harmonic spectrum of 9/8 base configuration [5]

It is worth noting that the harmonic order with the higher Ampere-turns is not the first but the p_b^{th}, which is the fourth in this case, this is due to the fractional pole per phase per slot value, to which we refer as q.

For each harmonic order is possible to define the corresponding **harmonic winding factor** as:

$$k_{wv} = \frac{h_v}{w_{hv}} \tag{3.41}$$

Where h_v is the amplitude of the v^{th} harmonic order and w_{hv} is the harmonic weight. The harmonic weight is the current linkage created by a hypothetical phase winding, consisting of a single coil with the span equal to the v^{th} harmonic pole pitch, with the same total number of ampere-turns as in the normalized winding:

$$w_{hv} = \frac{2}{v}\int_{\alpha=0}^{\alpha=2\pi}\sqrt{\Theta^2(\alpha)d\alpha} = \frac{2}{v}\frac{\Theta_{max}\cdot s}{2\pi} = \frac{Q_s}{vm\pi} \tag{3.42}$$

Where:

- Q_s number of slot per stator
- m number of phases
- $s = Q_s/m$ number of slots per phase
- Θ_{max} is the current linkage of a one turn coil which is 1 because of the normalization

Combining (3.41) and (3.42):

$$k_{wv} = h_v v\pi\frac{m}{Q_s} \tag{3.43}$$

in figure 3.21 are reported the first twenty-five harmonic winding factors calculated form the values in figure 3.20 using Eq 3.43.

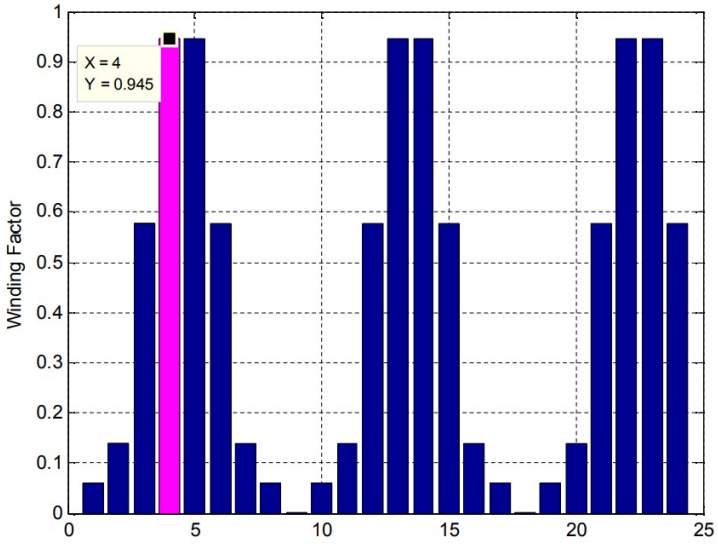

Figure 3.21: Harmonic winding factor of the 9/8 base configuration [5]

once the harmonic winding factors are known is possible to calculate the **harmonic leakage factor**, for traditional distributed windings:

$$\sigma_\delta = \sum_{v=-\infty;v\neq 1}^{v+\infty} (\frac{k_{wh}}{v \cdot k_{w1}})^2 \tag{3.44}$$

while for fractional windings:

$$\sigma_\delta = \sum_{v=-\infty;v\neq p_b}^{v+\infty} (p_b \cdot \frac{k_{wh}}{v \cdot k_{wp_b}})^2 \tag{3.44}$$

The term $v = p_b$ represents the synchronous harmonic order, and thus, the magnetizing inductance L_m component. The phase inductance can be expressed as:

$$L_s = L_m + L_\delta + L_{\sigma c} = L_m(1 + \sigma_\delta) + L_{\sigma c} \tag{3.45}$$

$$L_s = L_m \cdot \sum_{v=1}^{v=+\infty} (p_b \cdot \frac{k_{wv}}{v \cdot k_{wp}})^2 + l_{\sigma c} \tag{3.46}$$

in the figure below are reported the most common slot/pole configurations and for each of them the harmonic leakage factor has been calculated.

Qs \ 2p		4	6	8	10	12	14	16	18	20
6	q	1/2		1/4	1/5		1/7	1/8		1/10
	k_{wp}	0.866		0.866	0.5		0.5	0.866		0.866
	m_c	-0.5		-0.5	0		0	-0.5		-0.5
	σ_δ	**0.46**		**4.8**	**26**		**53**	**22**		**36**
9	q	3/4	1/2	3/8	3/10	1/4	3/14	3/16		3/20
	k_{wp}		0.866	0.945	0.945	0.866	0.617	0.328		0.328
	m_c		-0.5	-0.039	-0.039	-0.5	-0.039	-0.039		-0.039
	σ_δ		**0.46**	**1.2**	**2.4**	**4.8**	**15**	**71**		**112**
12	q	1	2/3	1/2	2/5		2/7	1/4		1/5
	k_{wp}			0.866	0.933		0.933	0.866		0.5
	m_c			-0.5	0		0	-0.5		0
	σ_δ			**0.46**	**0.96**		**2.9**	**4.8**		**26**
15	q	1 1/4	5/6	5/8	1/2		5/14	5/16		1/4
	k_{wp}				0.866		0.951	0.951		0.866
	m_c				-0.5		-0.013	-0.013		-0.5
	σ_δ				**0.46**		**1.4**	**2.1**		**4.8**
18	q	1 1/2	1	3/4	3/5	1/2	3/7	3/8		3/10
	k_{wp}					0.866	0.902	0.945		0.945
	m_c					-0.5	0	-0.039		-0.039
	σ_δ					**0.46**	**0.83**	**1.2**		**2.4**
21	q	1 3/4	1 1/6	7/8	7/10	7/12	1/2	7/16		7/20
	k_{wp}						0.866	0.89		0.953
	m_c						-0.5	-0.007		-0.007
	σ_δ						**0.46**	**0.8**		**1.5**
24	q	2	1 1/3	1	4/5	2/3	4/7	1/2		2/5
	k_{wp}							0.866		0.933
	m_c							-0.5		0
	σ_δ							**0.46**		**0.96**
27	q	2 3/4	1 1/2	1 3/8	9/10	3/4	9/14	9/16	1/2	9/20
	k_{wp}								0.866	0.877
	m_c								-0.5	-0.004
	σ_δ								**0.46**	**0.75**

Unbalanced radial magnetic pull Invalid configurations

Figure 3.22: Leakage factor for different slot/pole configurations [6]

3.5 Choice of pole/slot combination

Established that in a three-phase machine the number of slots must be a multiple of three, the combination between the number of slots in the stator and poles in the rotor influences deeply the motor behaviour in many ways, the most important ones are:

- Winding factor k_{w1}

- The harmonic air-gap leakage factor σ_δ

- The cogging torque harmonic order

- The working magneto motive force harmonic order

There are some common accepted rules to follow when choosing the right pole/slot combination:

- The winding factor of the working harmonic order should be the highest possible

- The minimum common multiple between Q_s and $2p$ should be the highets possible since this value corresponds to the first harmonic order of cogging torque different to zero

- The maximum common divider between Q_s and $2p$ should be an even number, that ensures a better balancing of the magnetic forces inside the motor.

Not every pole/slot combination is feasible since the torque has to be generated in every angular position of the rotor. In fig.3.23 are reported the most common pole/slot combinations

Number of slots	Pole pairs (n_p)									
n_{slots}	6	7	8	9	10	11	12	13	14	15
9	0.25	0.21	0.19	0.17	0.15	0.14	0.13	0.12	0.11	0.10
12	X	0.29	0.25	0.22	0.20	0.18	0.17	0.15	0.14	0.13
15	0.42	0.36	0.31	0.28	0.25	0.23	0.21	0.19	0.18	0.17
18	0.50	0.43	0.38	X	0.30	0.27	0.25	0.23	0.21	0.20
21	0.58	0.50	0.44	0.39	0.35	0.32	0.29	0.27	0.25	0.23
24	X	0.57	0.50	0.44	0.40	0.36	X	0.31	0.29	0.27
27	0.75	0.64	0.56	0.50	0.45	0.41	0.38	0.35	0.32	0.30
30	0.83	0.71	0.63	0.56	0.50	0.45	0.42	0.38	0.36	X
33	0.92	0.79	0.69	0.61	0.55	0.50	0.46	0.42	0.39	0.37
36	1.00	0.86	0.75	X	0.60	0.55	0.50	0.46	0.43	0.40
39	1.08	0.93	0.81	0.72	0.65	0.59	0.54	0.50	0.46	0.43
42	1.17	1.00	0.88	0.78	0.70	0.64	0.58	0.54	0.50	0.47
45	1.25	1.07	0.94	0.83	0.75	0.68	0.63	0.58	0.54	0.50
48	X	1.14	1.00	0.89	0.80	0.73	X	0.62	0.57	0.53
51	1.42	1.21	1.06	0.94	0.85	0.77	0.71	0.65	0.61	0.57
54	1.50	1.29	1.13	1.00	0.90	0.82	0.75	0.69	0.64	0.60
57	1.58	1.36	1.19	1.06	0.95	0.86	0.79	0.73	0.68	0.63
60	X	1.43	1.25	1.11	1.00	0.91	0.83	0.77	0.71	X
63	1.75	1.50	1.31	1.17	1.05	0.95	0.88	0.81	0.75	0.70
66	1.83	1.57	1.38	1.22	1.10	1.00	0.92	0.85	0.79	0.73
69	1.92	1.64	1.44	1.28	1.15	1.05	0.96	0.88	0.82	0.77
72	2.00	1.71	1.50	X	1.20	1.09	1.00	0.92	0.86	0.80
75	2.08	1.79	1.56	1.39	1.25	1.14	1.04	0.96	0.89	0.83
78	2.17	1.86	1.63	1.44	1.30	1.18	1.08	1.00	0.93	0.87
81	2.25	1.93	1.69	1.50	1.35	1.23	1.13	1.04	0.96	0.90
84	X	2.00	1.75	1.56	1.40	1.27	1.17	1.08	1.00	0.93
87	2.42	2.07	1.81	1.61	1.45	1.32	1.21	1.12	1.04	0.97
90	2.50	2.14	1.88	X	1.50	1.36	1.25	1.15	1.07	1.00
93	2.58	2.21	1.94	1.72	1.55	1.41	1.29	1.19	1.11	1.03
96	X	2.29	2.00	1.78	1.60	1.45	X	1.23	1.14	1.07

Figure 3.23: Pole/Slot combinations [4]

- Configuration in which the torque is not produced in every rotor position
- The number of slots per pole per phase (q) is equal to 1.5
- Fractional concentrated winding witch $N_{slot} = N_{pole} \pm 2$ or $N_{slot} = N_{pole} \pm 1$
- Concentrated winding with q 0.5
- Fractional q with a period of 2 pole pairs (q = 0.75, 1.25, . . .)
- Integer q

The combination slot/pole is chosen in order to provide an inductance large enough to have the lower short circuit current I_{ch} keeping in mind that a too large inductance may lead to a way too small power factor. According to figure 3.22 a very good choice can be the configuration composed by 18 slots and 16 poles.

3.6 Stator Dimensioning

Once the number of slots has been chosen is possible to define the slot and tooth main dimensions. The main factors that influence the slot dimensioning are:

- Number of conductors in a slot n_{cs}
- Maximum current density admissible
- Fill factor desired k_{fill}

in figure 3.24 below are reported the parameters used for describing the main slot dimensions.

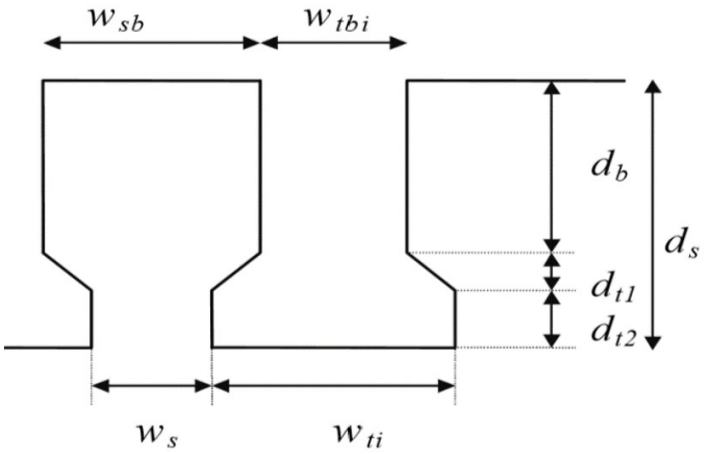

Figure 3.24: Main mechanical parameters of the slot and the tooth

For this preliminary step it has been decided to design the slot as rectangular, therefore $w_{sb} = w_s$. The stator has a double layer concentrated winding, this means that every tooth has a coil wounded around its body.

According to 3.3.5:

$$N_1 = \frac{\pi D_{out}(1 + k_d)A_m}{4m\sqrt{2}I_a} \tag{3.26}$$

N_1, obtained in 3.3.5, must be rounded so that it becomes a multiple of the number of poles per phase so that in every slot the number of windings is an integer. Since Q_s is known (and so the number of teeth) and there is one coil per tooth we know the number of coils per phase. In every slot there are double the number of winding per coil as it is easily deducible from figure 3.25 so that:

$$n_{cs} = \frac{N_1}{N_{coil_{phase}}} \cdot 2a \tag{3.47}$$

where a is the number of parallel conductors forming a single wire.

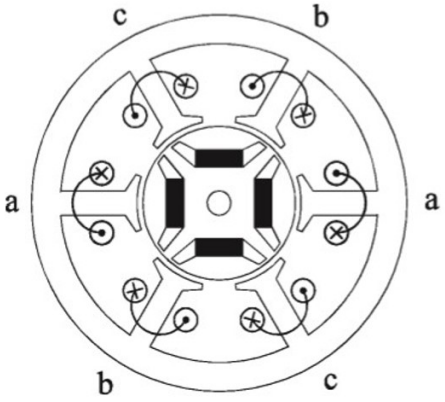

Figure 3.25: Typical double layer concentrated winding layout

The effective slot dimensioning starts by defining w_{ti} with the specific aim to avoid the tooth saturation while the machine is working. Under the hypothesis that all the magnetic flux in the air gap merges into the tooth it is possible to introduce the following equation:

$$w_{tbi} = \tau_{si} \frac{B_{g0}}{B_{tmax}} \tag{3.48}$$

Where τ_{si} is the internal slot pitch, B_{g0} is the magnetic flux density in the air-gap and $B_{t_{max}}$ is the maximum flux density allowed in the thooth internal path and depends on the materials used to build the stator.

The slot opening length is easily deducible from

$$\tau_{si} = w_{sb} + w_{tbi} \tag{3.49}$$

Now the slot depth has to be found and this can be done by estimating the total conductor cross section and fixing a desired filling factor. Assuming for this design step that every coil is formed by a single wire having an equivalent cross section calculable as:

$$A_c = \frac{I}{J_{s_{max}}} = \frac{A_s \cdot k_{fill}}{n_{cs}} \tag{3.50}$$

From 3.50, the equivalent conductor cross section depends on the maximum current density allowed and on the maximum phase current needed to provide

the desired torque. Once the slot area is calculated from 3.50, the slot depth is:

$$h_s = \frac{A_s}{w_{sb}} \tag{3.51}$$

3.7 Rotor Dimensioning

The rotor main dimensions have been fixed already in 3.3.3. In this section is reported the procedure to dimension the magnets that the rotor has to contain.

3.7.1 Permanent magnet design

The permanent magnets performance is heavily influenced by the working temperature of the motor. The residual flux density and the coercitive magnetic field of the magnet is given, in function of the temperature in the following equations:

$$B_r = B_{r_{20}}[1 + \frac{\alpha_B}{100}(\theta_{PM} - 20)] \tag{3.52}$$

$$H_c = H_{c_{20}}[1 + \frac{\alpha_H}{100}(\theta_{PM} - 20)] \tag{3.53}$$

Where $B_{r_{20}}$ and $H_{r_{20}}$ are the residual flux density and the coercitive magnetic field in ambient temperature conditions, here fixed at $20°C$. α_B and α_H are temperature coefficients that depend on the PM material.

The permanent magnet height h_m has to be big enough to guarantee a proper flux density B_g in the air gap.

$$h_m = \mu_{rrec}\frac{\sigma_{lM}B_g}{B_r - \sigma_{lM}B_g}g \tag{3.54}$$

As indicated in 3.54 the magnet height depends on σ_{lM} which is the magnet leakage factor, unfortunately this factor is very difficult to calculate and depends on many factors including the nature of the magnetic circuit. A proper value of σ_{lM} might be 1.15 according to [3].

Since the permanent magnet has a permeability similar to the air one, it contributes to the total air gap width. The equivalent air gap considering the magnets height is:

$$g_{eq} = g + \frac{h_m}{\mu_{rrec}} \tag{3.55}$$

Finally, known the fraction of pole pitch α_i occupied by the magnet, the magnet width is:

$$w_m = \alpha_i \tau \tag{3.56}$$

3.8 Design results

At the end of the design procedure the motor presents the following layout.

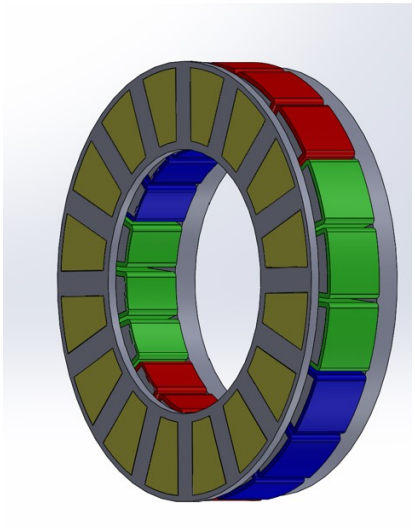

Figure 3.26: Layout of the main motor geometry

It is worth noting that the second stator has been neglected from the picture for a better comprehension of the final result.

Main dimensions	**Value**	**Symbol**
External diameter	$347[mm]$	d_{ext}
Internal diameter	$225[mm]$	d_{int}
Slot number	18	Q
Pole number	16	P
Electrical data		
DC-link voltage	$400[V]$	V_{dc}
Phase to star point voltage	$163[V]$	$V_{1_{rms}}$
Phase current	$323[A]$	I_a
Nominal frequency	$473[Hz]$	f_r
Synchronous inductance	$0.187[mH]$	Ls
Phase resistance	$29[m\Omega]$	$R_{1_{ac}}$
Windings		
Windings per phase	18	N_1
Wire cross section	$65[mm^2]$	s_a
Permanent magnet		
Remanent magnetic flux density	$1.2[T]$	B_r
Magnet height	$7.6[mm]$	h_m
Magnet height	$7.6[mm]$	h_m
Mechanical data		
Base speed	$370[rad/s]$	ω_b
Iron weight	$31.7[kg]$	m_{iron}
Copper weight	$6.8[kg]$	m_{copper}
Total active material weight	$38.52[kg]$	m_{tot}

Table 3.3: Vehicle and motor design data

Chapter 4

Main Electo-Magnetical Quantities

In this chapter the main quantities of the designed machine are analytically evaluated

4.1 Resistance

In this section are explained the main procedures to make an analytical computation of the motor phase resistance given the main geometry.

4.1.1 DC Resistance

The coil resistance in a DC regime can be written as:

$$R_{DC} = \frac{N_1 l_{av}}{a_p a_w \sigma s_a} \tag{4.1}$$

Where:

- N_1 = number of windings per phase
- l_{av} = total phase windings length
- a_p = number of parallel paths
- a_w = number of parallel conductors
- σ = conductor resistivity
- s_a = conductor cross section

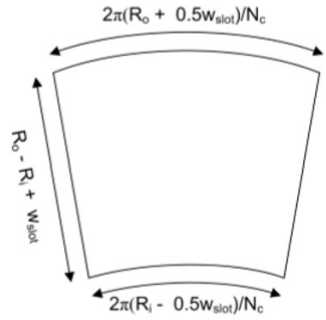

Figure 4.1: Winding length, analytical approximation [8]

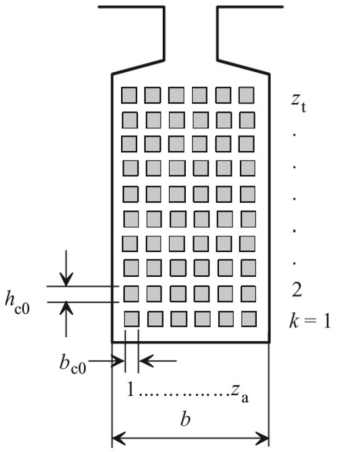

Figure 4.2: Positional parameters of the conductors in a slot [16]

When concentrated winding technology is used, the analytical evaluation of the total phase winding length can be tricky because of the end windings design. A good approximation of l_{av} can be done considering the outer end windings to be long as the outer tooth circular arc plus an half of the slot width, on the other hand the inner end winding can be considered long as the inner tooth circular arc minus a half of the slot width as shown in figure 4.1.

4.1.2 AC Reistance

Since the motor works with alternating current is necessary to include the contribute of skin and proximity effects in the phase resistance analysis. Considering the coil conductors positioned as shown in figure 4.2. The AC

resistance can be expressed as:

$$R_{AC} = k_R R_{DC} \tag{4.2}$$

Where:

$$k_R = \phi(\xi) + \frac{z_t^2 - 1}{3}\psi(\xi) \tag{4.3}$$

$$\phi(\xi) = \xi\frac{sinh(2\xi) + sin(2\xi)}{cosh(2\xi) - cos(2\xi)} \tag{4.4}$$

$$\psi(\xi) = 2\xi\frac{sinh(\xi) - sin(\xi)}{cosh(\xi) + cos(\xi)} \tag{4.5}$$

The parameter ξ is called **slot reduction factor** and takes into account the mutual position of the coil conductors in the slot.

$$\xi = \alpha h_{c_0} = h_{c0}\sqrt{\frac{1}{2}\omega\mu_0\sigma_c\frac{z_t b_{c_0}}{b}} \tag{4.6}$$

It is worth noting that the currents flowing into the parallel conductors have been neglected from the R_{AC} calculus as well as the the fact that in some slots the conductors belong to two different phases. The results obtained by 4.2 have to be considered as an approximation and needs to be confirmed by the FEA simulation.

4.2 Inductance

The machine inductance is difficult to calculate analytically, nevertheless exist many approximated models, the one used in this work of thesis is explained in this section. As said in 3.4.1 the machine synchronous inductance is the sum of two main components, the magnetizing inductance and the leakage inductance, the latter is the sum of four inductance parameters as well.

$$L_s = L_m + L_{ew} + L_u + L_d + L_\delta = L_m + L_\delta + L_{\sigma_c} = L_m(1 + \sigma_\delta) + L_{\delta_c} \tag{4.7}$$

4.2.1 Magnetizing and air gap leakage inductance

For an axial flux motor the magnetizing inductance is easily expressed as:

$$L_m = \frac{3}{2}m_1\mu_0\frac{1}{\pi}(\frac{N_1 k_w}{p})^2\frac{R_{out}^2 - R_{in}^2}{g'} \tag{4.8}$$

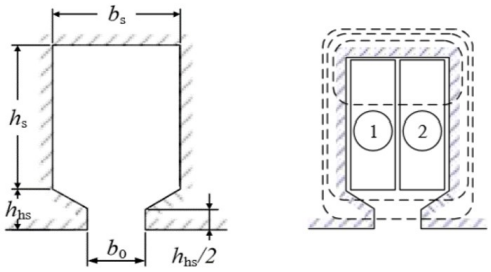

Figure 4.3: Parameters of the conductors position in slot [10]

where $\frac{3}{2}$ takes into account the mutual contribute of the other phases.

From 3.22 is now easy to calculate the airgap leakage inductance as

$$L_\delta = L_m \sigma_\delta \tag{4.9}$$

4.2.2 Slot leakage inductance

In the case under exam the conductors in the slots are placed as shown in figure 4.3

The slot leakage inductance is:

$$L_u = \frac{4m}{Q_s} \mu_0 l_{ef} N^2 \lambda_u \tag{4.10}$$

Where

$$\lambda_u = k_{1h} \cdot \frac{h_s}{3b_s} + \frac{k_{2h}}{2}\left(\frac{h_{hs}}{b_s - b_o} ln \frac{b_s}{b_o} + \frac{h_{hs}}{b_o}\right) \tag{4.11}$$

and with:

$$k_{1h} = k_{2h} = k_{2v} = 1 - \frac{|y_q - W|}{4q} \tag{4.12}$$

Where l_{eff} is the active length, W is the coil pitch which is 1 if concentrated windings are used and y_q is the number of slots per pole. It is worth noting that for a rectangular slot like the one designed in 3.6, $h_s = 0$

4.2.3 End winding leakage inductance

The leakage inductance component due to the end windings depends on their relative permeability. For the inner end connection:

$$\lambda_{e_{in}} \approx 0.17q\left(1 - \frac{2}{\pi}\frac{w_{c_{in}}}{l_{in}}\right) \tag{4.13}$$

For the outer end connection:

$$\lambda_{e_{out}} \approx 0.17q(1 - \frac{2}{\pi}\frac{w_{c_{out}}}{l_{out}}) \tag{4.14}$$

This equation has been deduced experimentally and:

- l_{in}; l_{out} = inner and outer end winding length
- $w_{c_{in}}$; $w_{c_{out}}$ = inner and outer coil span

The whole relative permeability is the sum of the two:

$$\lambda_e = \lambda_{e_{in}} + \lambda_{e_{out}} \tag{4.15}$$

Finally:

$$L_{ew} = \frac{2\mu_0}{pq}(l_{in}\lambda_{e_{in}} + l_{out}\lambda_{e_{out}}) \tag{4.16}$$

4.2.4 Tooth leakage inductance

The tooth leakage inductance is given by the following equation:

$$L_d = \frac{4m}{Q_s}\mu_0 N_s^2 l_{eff} k_2 \lambda_{tt} \tag{4.17}$$

Where λ_{tt} depends on the slot opening w_{sb} and on the air gap legth g:

$$\lambda_{tt} = \frac{1}{2\pi}[ln(\frac{\delta^2}{w_{sb}^2} + \frac{1}{4}) + 4\frac{\delta}{w_{sb}}arctan\frac{w_{sb}}{2\delta}] \tag{4.18}$$

with:

$$k_2 = \frac{1+g}{2} \tag{4.18}$$

4.3 Losses

In order to guarantee a proper functioning of the motor an high efficiency must be reached, this means that the electromagnetic losses must be kept as low as possible. In this section the main procedure to compute the motor losses is reported.

4.3.1 Joule losses

The Joule losses are given by:

$$P_{Joule} = 3R_{AC}I_{eff} \tag{4.19}$$

4.3.2 Iron losses

The iron losses can be modelled as the sum of three different values:

$$P_{iron} = P_h + P_{eddy} + P_a \tag{4.20}$$

where:

- P_h are the **hysteresis losses**. The hysteresis losses are considered to be related to the magnetic domains movement and rotation, as well as material grain's composition and size. The hysteresis losses are well known to be proportional to the area that has the B-H curve as contour.

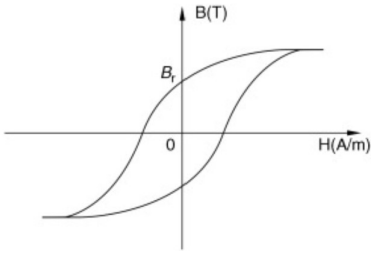

Figure 4.4: Typical B(H) curve of a ferromagnetic material

- P_{eddy} are the **eddy current losses**. The eddy current losses occur when the ferromagnetic material is subject to a time varying magnetic field that causes the flowing of undesired currents in the material.
- P_a are the **additional losses** that take into account some side magnetic effects.

The motor stator is made of **soft magnetic compound** (**SMC**). The manufacturer gives a formula (equation 4.21) to predict the losses per kilogram of material (specific losses, here indicated by the lowercase letters). The formula is applicable, according to the normative CEI/IEC 60404-6:2003 on a ring sample with the following dimensions:

Outer diameter	**Inner diameter**	**Height**
$55mm$	$45mm$	$5mm$

Table 4.1: Ring sample dimensions

$$p_{Iron} = p_h + p_{eddy} + p_a = K_h f B^{1.75} + K_{ep} f^2 B^2 + \sigma_{SMC} \frac{B^2 f^2 d^2}{1.8 * \rho_{SMC}} \tag{4.21}$$

with:

- K_h = hysteresis constant depending on the material
- K_{ep} = Eddy currents constant depending on the material
- ρ_{SMC} = SMC volumetric density
- σ_{SMC} = SMC conductibility
- d = smallest length of the section where the eddy current flows

In equation 4.21 can be identified three different loss phenomena:

4.3.3 Magnet losses

Due to the slots opening the magnets see an alternate magnetic flux density at the frequency of:

$$f_{sl} = N_{slot} pn \tag{4.24}$$

Where n is the number of turns per second of the rotor. The flux density component due to the slot opening has an amplitude of:

$$B_{sl} = a_{sl} \beta sl k_c B_{avg} \tag{4.25}$$

Where:

$$a_{sl} = \frac{4}{\pi}(0.5 + \frac{\Gamma^2}{0.78 - 2\Gamma^2}) sin(1.6\pi\Gamma) \tag{4.26}$$

$$\beta_{sl} = 0.5(1 - \frac{1}{\sqrt{1 + k^2}}) \tag{4.27}$$

$$\Gamma = \frac{w_{sl}}{\tau_s} \tag{4.28}$$

$$k = \frac{w_{sl}}{g'} \tag{4.29}$$

where τ_s is the average slot pitch and k_c is the Carter factor. It is worth noting that by doubling the slot opening, the losses in the magnet become more than twice (see fig.4.5).

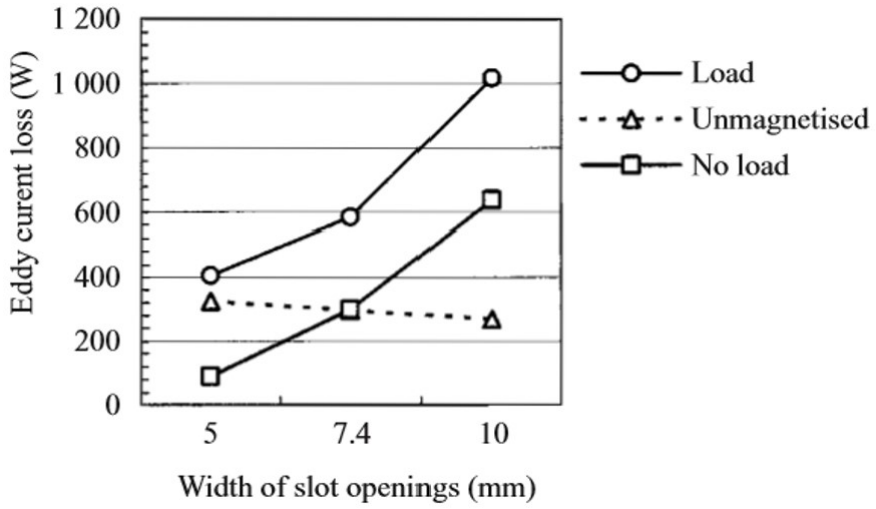

Figure 4.5: Magnet losses in function of w_{sl} [13]

Chapter 5

Constructive analysis

5.1 Stator

The choice of the stator material influences deeply the machine behaviour. The most important characteristics to look for to choose the material are the resistivity and the hysteresis function, the former has to be high enough to guarantee low eddy current losses, the latter has to be compatible with the currents injected in the motor phases preventing saturation in the narrower regions such as theeth and slots.

In the most common radial flux machines the magnetic field crossing the stator has the radial directions as the main one, for this reason **electrical steel** well suits the application needs. Electrical steel usually is a magnetic isotropic material which means that the permeability is the same in every direction. Thanks to particular processes, electrical steel can be produced with oriented-grain technology that favor the passage of the flux in one particular direction, when this occurs it is said that the material is anisotropic.

5.1.1 Soft magnetic compound

The main drawback of using electrical steel is that, in order to avoid uncontrolled eddy currents in the material, a **lamination** is needed. In case of an axial flux machine the lamination process can be tricky due to the complex geometry of the stator, in this case it is preferable to use **soft magnetic compound** (**SMC**). The aim of the SMC is to provide a competitive magnetic material with high electrical resistivity, this can be achieved using iron powder particles insulated as described in the figure below.

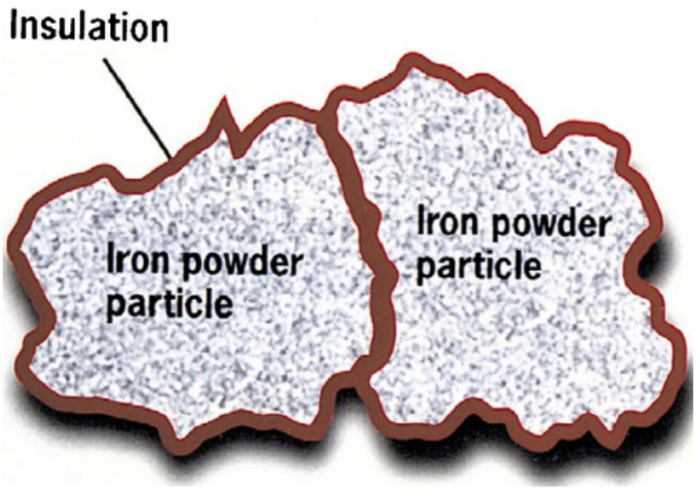

Figure 5.1: Soft magnetic compound structure [17]

There are two basic types of SMC that are commonly used, depending on the application:

- **Ferrimagnetic materials**, are based on ceramic metal oxides, such as ferrites and well suite applications in which frequencies are in the range of a few kHz to over $80MHz$.

- **Ferromagnetic materials**, based on iron and nickel, they are used in applications in which the frequency is lower than $2kHz$. They are usually employed in electrical machines.

The main drawback of SMC is the lower permeability if compared to electrical laminated steel so while the losses in a SMC core are lower, it has to be considered an increase of the material overall volume to ensure a proper flux density. In figure 5.4 is shown the applicability regions of both SMC and electrical steel.

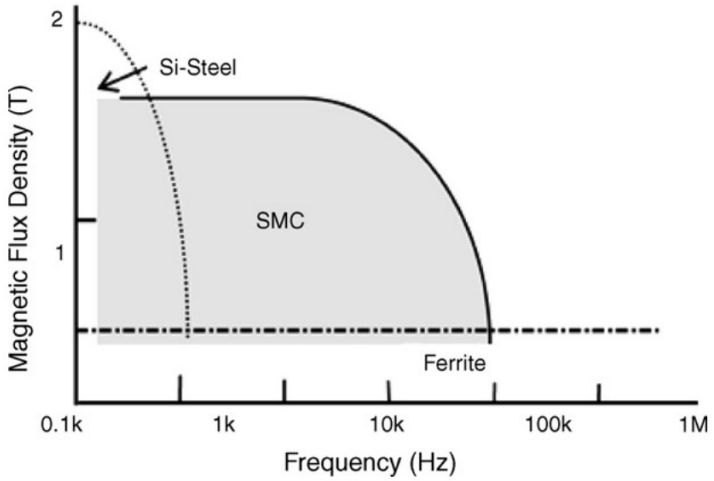

Figure 5.2: The applicable regions for soft magnetic materials used in AC magnetic fields [17]

The losses in the stator SMC core can be divided into two main components:

- **Histeresis losses**: Is the main loss component at low frequencies, it can be reduced by mean of larger particle size, higher purity of the iron in the particles and stress relieving heat treatment

- **Eddy current losses**: They are the losses due to the induction of currents isinde the core by the mean of magnetic fields varying in time, with respect to the core itself. To overcome the issue an insulation coating can be added to the particles (see figure 5.1). On the other hand the small non-magnetic distances between every particle act as an air gap and decrease the permeability of the bulk material.

Soft magnetic composites are produced by traditional powder compaction techniques followed by a heat treatment at low temperatures which does not destroy the insulating layer between the iron particles. Different magnetic and mechanical properties are obtained depending on binder, lubricant additives and organic coatings on the iron particles as well as warm or cold compaction. In the figure below is reported the main properties change of the material due to the different manufacturing procedure adopted:

	I	II	III	IV	V
Permeability	↑	↓	↓	↑	↑
Maximum flux density	↑	↓	↓	↑	↑
Coercivity	↑	–	–	↑	↓
Resistivity	↓	↑	↑	↓	↓
Thermal conductivity	↑	↓	↓	↑	↑
Strength	↓	↓	↑	↑↓[a]	↑

Figure 5.3: SMC characteristics change due to manufacturing choices:(I) Increasing particle size; (II) addition of lubricant; (III) addition of binder; (IV) increasing compaction pressure; (V) heat treatment. [17]

As it can be seen high permeability and high resistivity, which are the most important characteristics, are always in conflict no matter what manufacturing approach is used. The challenge is to find the optimal breakeven point. Considering what has been reported in subsection 5.1.1, the following material has been chosen to form the stator core:

Somaloy 130i 5P	**Property name**	**Value**
Magnetic properties	$B@4000A/m$	$1.14[T]$
	$B@10000A/m$	$1.47[T]$
	H_c	$153[A/m]$
	$\mu_{r_{max}}$	350
Electrical properties	ρ	$20000\mu\Omega m$

Table 5.1: Somaloy 130i 5P main characteristics

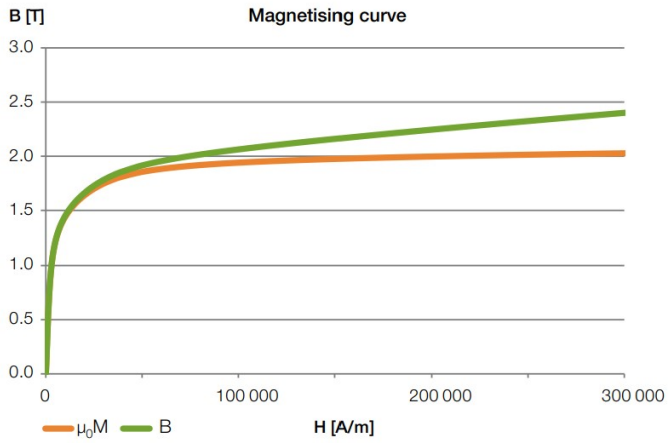

Figure 5.4: B-H curve of the Somaloy 130i 5P

5.1.2 SMC manufacturing process

The manufacturing process used to obtain the SMC core influences deeply the magnetic and mechanical performances of the material. The process is usually divided into three steps:

- **Powder production**: provided by the material company.
- **Powder compaction**: to achieve the desired core geometry.
- **Heat treatment**: to guarantee the mechanical properties.

Although there are different manufacturing methods that include the three steps reported above, the only one suitable for electrical machines is the so called **die compaction**. Figure 5.5 reports the characteristics of the tool used in die compaction. The tool is composed of three parts:

- **Upper die**
- **Bottom die**
- **Cavity die**

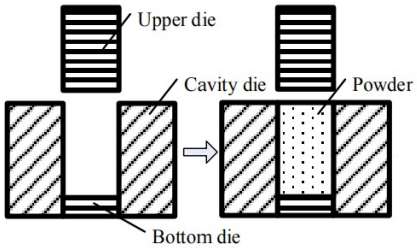

Figure 5.5: Die compaction tool

After the compacting process, the SMC cores are very fragile. The **heat treatment** can improve the mechanical strength of the compact SMC core but also can eliminate the defects in the core resulted by the compacting process. Usually the heat treatment has the following trend:

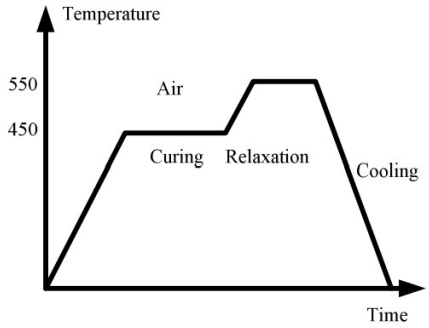

Figure 5.6: Heat treatment process of the compact SMC core

5.1.3 Windings technology

The choice of the wire diameter is not a trivial task because it assumes that the value of the maximum **current density J** inside the machine is known. The maximum current density allowable influences deeply the efficiency of the machine since the copper losses P_{cu} in a winding are proportional to the square of J and to the copper mass m_{cu}. Assuming the motor dimensions (diameter, lenght ecc.) to be variable over the scale λ, it can be said that:

$$P_{cu} \propto J^2 m_{cu} \propto J^2 \lambda^3 \tag{5.1}$$

The thermal resistance R_{th} between the conductors and the teeth is:

$$R_{th} = \frac{d_i}{\lambda_i S_i} \tag{5.2}$$

where d_i is the thickness of the slot insulation which is independent of the machine size, hence independent of λ. λ_i is the thermal conductivity of the insulation and S_i is the area of the slot wall, thus:

$$R_{th} \propto \frac{1}{\lambda^2} \tag{5.3}$$

Now, the temperature difference between the copper and the stator core is:

$$\Delta T = P_{cu} R_{th} \propto J^2 \lambda \tag{5.4}$$

so, for a fixed temperature difference:

$$J^2 \lambda = constant \tag{5.5}$$

Finally:

$$J \propto \frac{1}{\sqrt{\lambda}} \tag{5.6}$$

Equation 5.6 shows that small machines tolerate higher current densities better than large ones. According to [16] the typical values of J for a PMSM machine are $4 \div 6.5 \times 10^6 A/m^2$. $J = 10 \times 10^6 A/m^2$ has been chosen, assuming that the cooling system is based on water flowing over the windings end connections.

To obtain the desired torque of $350Nm$ a phase current I_a of $330A$ is necessary. Considering the winding made by a single wire, its cross section must be:

$$A_{cu} = \frac{I_a}{J} = 33mm^2 \tag{5.7}$$

There are two main types of copper wire to chose from to form a coil:

- **Pull-in wire**: the conductors are made of thin circular wires connected in parallel. The small thickness of the wires allows to avoid skin effect but has a bad influence on the filling factor. Besides, due to their mutual position in the slot, the conductors in parallel are subject to undesired induced EMF. Finally the possibility to divide a single conductor into many smaller ones gives modularity to the coil project. It is also possible to improve the fill factor by adopting small square (or rectangular) wires, as shown in figure 5.7. Given the same cross section, the square wire is less demanding in terms of space occupied.

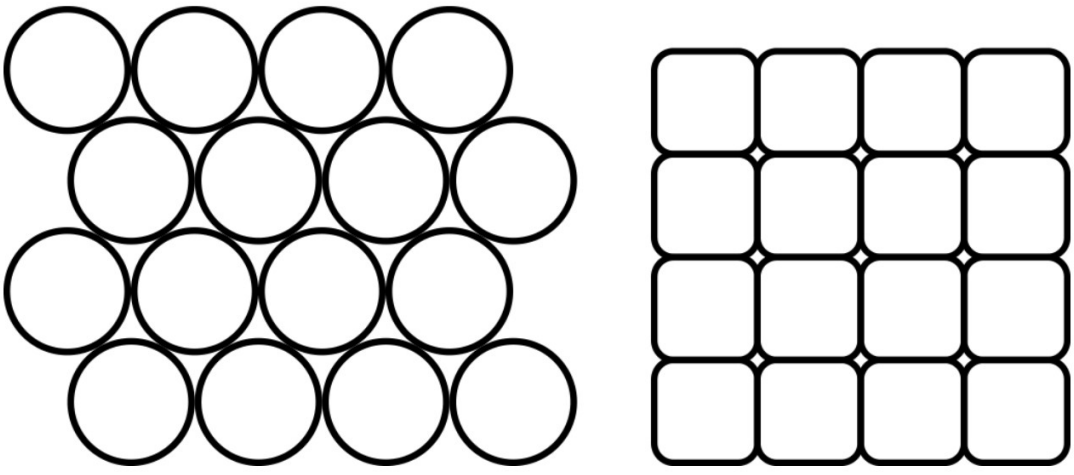

Figure 5.7: Square and round wires with the same cross section occupy different space

- **Hairpin winding**: the conductors are large rectangular bars connected in series. The fill factor is higher than in the round pull-in wire. Large bars allow a better thermal conductance of the losses. The serial connection of the bars avoids circular currents. The number of turns is smaller than a pull-in winding machine, so it is hard to modify the winding to fit into another specification. Due to the large size of the conductors, hairpin windings are more sensitive to skin effect than pull in windings

From equation 5.7 it has been calculated a wire cross section of $33mm^2$, this value is too big for a proper design, the author's choice is to divide the conductor in several Pull-in wire with square section to improve the copper fill factor and to decrease the skin effect. The copper wire is usually provided with a thin insulating coat, the wire is then called **enamelled**. A particular category of enamelled copper wires is the **self bonding** enamelled wire which is provided with a secondary insulation varnish layer made of bondable material which is usually thermoplastic and bonds the wires surfaces with each other once heated at the bonding temperature.

SEPL Polyesterimide Enamelled	**Property name**	**Value**
	Insulation class	180
	Square cross section	$3.3mm$
	Number of parallel conductors	6

Table 5.2: Coil wire characteristics

5.2 Rotor

Thanks to his peculiar configuration, the double stator internal rotor axial flux motor does not need a ferromagnetic rotor since the flux naturally goes from one stator to another. The use of an **ironless rotor** brings many advantages:

- **Less permanent magnet material needed**: The common ferromagnetic rotor needs permanent magnets on both sides to allow the flux to flow properly in the air gaps (see figure 5.8). On the other hand the ironless rotor does not influence the flux which moves freely through the airgaps as shown in figure 5.9. In the ironless configuration, the magnets can be inserted directly inside the rotor without creating anisotropy with a saving in magnetic material.

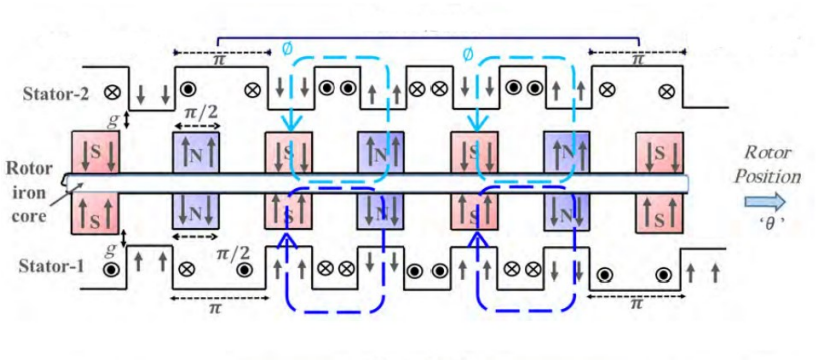

Figure 5.8: Section of a double stator interior magnetic rotor with evidence of the flux path[18]

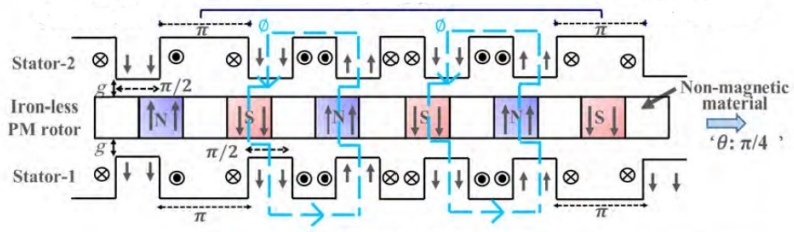

Figure 5.9: Section of a double stator interior ironless rotor with evidence of the flux path[18]

- **Less losses and torque ripple**: The motor with an ironless rotor had superior power capacity and reduced cogging torque and torque ripples compared to the iron core motor. An iron core rotor can be subject to saturation because of the higher currents in the windings and the considerable size of the magnets. This saturation can become a source of asymmetric flux distribution as well as a heat production that drives the operating point of the magnets toward or below the knee point on the BH curve. An iroless rotor is not subject to eddy current losses and this increases the efficiency of the whole motor.

The ironless rotor can be made of many different nonmagnetic materials, the most common solutions are epoxy resin and stainless non-magnetic steel. For what concern **epoxy resin** the main advantage is the lightness of the material that drastically drops the moment of inertia allowing a better dynamic performance. On the other hand the epoxy resin has poor mechanical properties, this may lead to small fractures due to mechanical stress and

for this reason an exterior boundary must be designed. The **non-magnetic steel** is, instead, robust and can bear high speed working points easily, for this reason non-magnetic steel has been chosen to form the machine rotor.

5.2.1 Stainless steel

There are several families of stainless steels with different physical properties. The magnetic properties of stainless steel depend on the elements added into the alloy. The most common stainless steels are austenitic with a high chromium content and nickel is also added. It is the nickel which modifies the physical structure of the steel and makes it theoretically non-magnetic.

The 316 stainless steel is a molybdenum-alloyed steel and is negligibly responsive to magnetic fields, for this reason it can be used in applications where a non-magnetic metal is required. The alloy is formed by the following materials:

Type 316	**Material name**	**Concentration**
	Carbon	0.08% max
	Manganese	2.00% max
	Phosphotus	0.045% max
	Sulfur	0.030% max
	Silicon	1% max
	Chromium	$16.00 - 18.00\%$
	Molybdenum	$2.00 - 3.00\%$

Table 5.3: 361 stainless steel alloy chemical composition

5.2.2 Permanent magnets

Assuming a ring made of a permanent magnetical material, the ring is magnetized until its saturation point, than the magnetizing source is removed. Although the external field strength is removed, a remanence flux density B_r remain in the ring. When the magnet is open forming an air gap δ. Measuring the field strength H_δ, since there is no current:

$$\oint \vec{H}d\vec{l} = H_{PM} * h_{PM} + H_\delta * \delta = 0 \tag{5.7}$$

The field strength of the magnet is:

$$H_{pm} = -\frac{\delta}{h_{pm}} H_\delta \tag{5.8}$$

Equation 5.8 shows that the influence of an air gap corresponds to the situation in which an unopened permanent magnet ring is magnetized in a negative direction with the field strength H_{PM}.

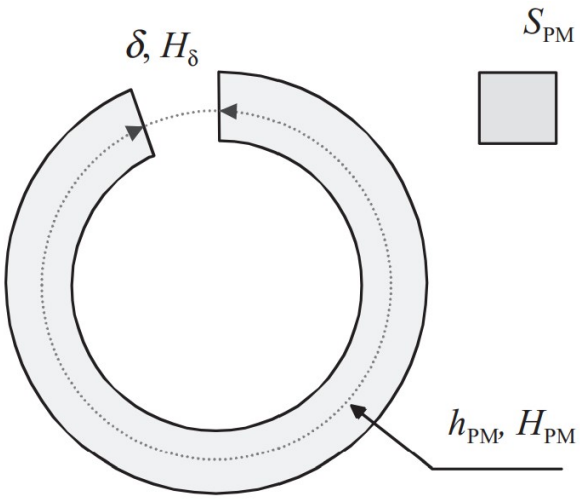

Figure 5.10: Definition of the field strength of an opened permanent magnet ring [16]

On the characteristic curve of the ring material (Figure 5.11), the operating point has moved from B_r to the point A (called a base point), where the field strength $H_A = H_{PM}$. Shortening the air gap, the operating point moves along the **reversible magnetizing** line $A\ B'_A$, called an operation line segment. Closing the ring again, the new remanence flux density will be B'_A, which is lower than the original remanence flux density B_r.

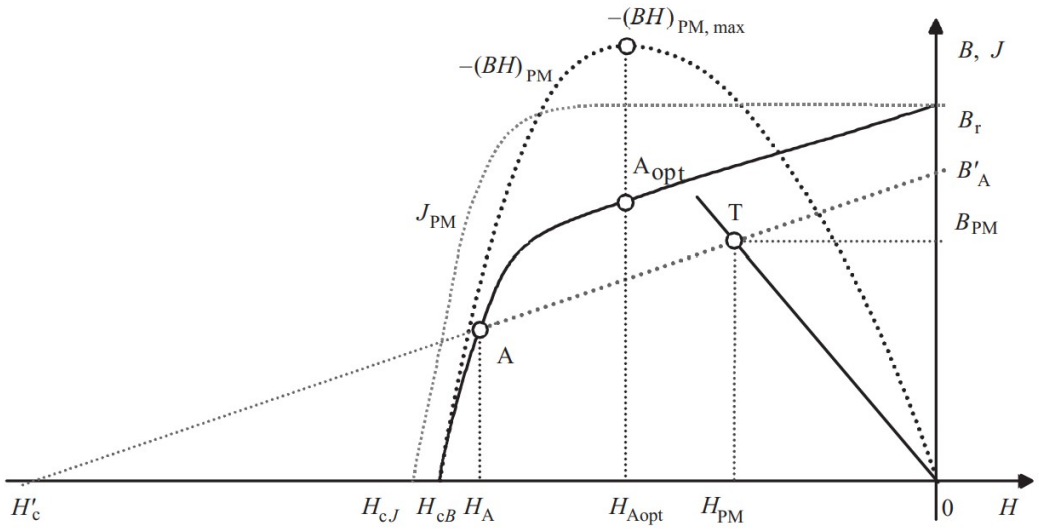

Figure 5.11: Typical demagnetization curve in a permanent magnet [16]

The decisive requirements for a good permanent magnet are:

- **High saturation point**: This leads to an high remanent flux density.
- **High Curier temperature**: Permanent magnets are very sensitive to temperature, the Curier temperature is defined as the temperature in which the material loses his permanent magnetic properties. An high Curier temperature means an higher loadability of the machine keeping the same cooling system.

The permanent magnet chosed for the application in a sintered NeFeB magnet with the following characteristics:

NeFeB N35	**Property name**	**Value**
Magnetic properties	Residual flux density B_r	$1.17 \div 1.25[T]$
	Coercitivity H_{cB}	$860 \div 950[kA/m]$
	Intrinsic coercitivity H_{cJ}	$955[kA/m]$
	Maximum energy HB_{max}	$263 \div 302[kJ/m^3]$
Thermal properties	Coeff. residual $\alpha(B_r)$	$-0.12\%/C^\circ$
	Coeff. coercitivity $\alpha(H_c)$	$-0.75\%/C^\circ$
	Curie temperature T_c	$310C^\circ$
Electrical properties	Electrical resistivity ρ	$180\mu\Omega cm$

Table 5.4: Sintered NeFeB characteristics

Chapter 6

Finite Element Analysis

The results obtained analytically in the previous chapters are now verified with a finite element analysis (**FEA)**. The tool used is COMSOL Multiphisics. The aim of the analysis is to evaluate:

- Back EMF (waveform and peak)
- Eddy current losses (magnets and iron)
- Joule losses
- Torque production

6.1 Model Geometry

The geometry obtained in section 3.8 presents some mesh issues. The high aspect ratio ($\frac{350mm}{1.3mm}$) in the air gap region leads to poor mashes so that a great number of extra fine thetraedral elements are needed. On the other hand when the number of elements in the mesh is too high the hardware computing power might not be enough with consequential forced shutdown of the software or a way to slow simulation. Moreover the sharp edges of the stator teeht leads to a coil geometry which does not fit the solver requirements, as a matter of fact the coil might be as round as possible to be solved properly. For these two reasons a change in the model geometry as been made to reach a satisfying mesh.

The inner radius of the stator back-iron has been reduced of $10mm$ while the outer radius has been increased of the same quantity to ensure a proper space for the meshes in the boundary between the stator yoke and the windings. The teeth have been rounded while maintaining the same fill factor in the slots, this allows a better meshing in the teeth and the windings and

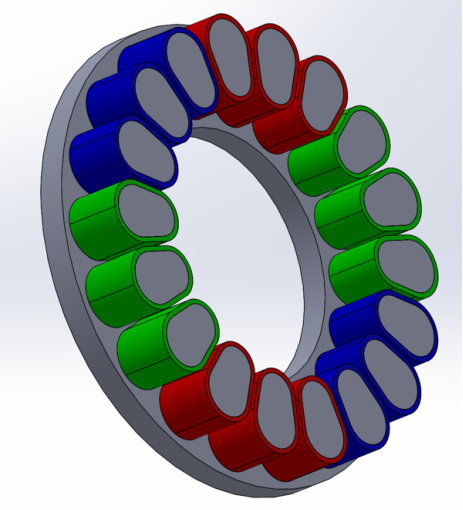

Figure 6.1: Geometry used for the meshing sequence

a better solution of the winding physic. Moreover the airgap has been increased to $g = 1.3mm$ to $g' = 4mm$ to ensure a good compromise between good mesh quality and low number of elements.

It is worth noting that, to ensure a proper analysis, while the air gap length increases for numeric reasons, the magnetic flux density field in the air gap must remain the same. This means that during the simulation, the remanent flux density of the permanent magnets has to be increased proportionally with the air gap length. The relation between the remanent flux density needed and the airgap length is expressed in the equation 6.1 whitch has been explained already in 3.7. Once the desired flux density in the air-gap B_g has been set, the remanent flux density needed is:

$$B_r = \frac{\sigma_{lm} B_g (h_m + \mu_{rrec} g')}{h_m} \tag{6.1}$$

It is worth noting that in equation 6.1 both B_r and σ_{lm} are unknowns and, as specified in 3.7, finding the value of σ_{lm} is not a trivial task. The strategy adopted is to use a first simulation in witch B_r is imposed by the user. At the end of the simulation the value of B_g is easily deducible and so it is possible to solve 6.1 with respect to σ_{lm}. Once σ_{lm} is known, imposing a desired B_g in the air gab (see also 3.3.1), equation 6.1 can be solved with respect to B_r. The result obtained represents the value of remanent flux density needed to have the same airgap flux density when airgap length is increased from g to g'. Another valid strategy might be to maintain the same remanent flux density and modify the magnet height h_m.

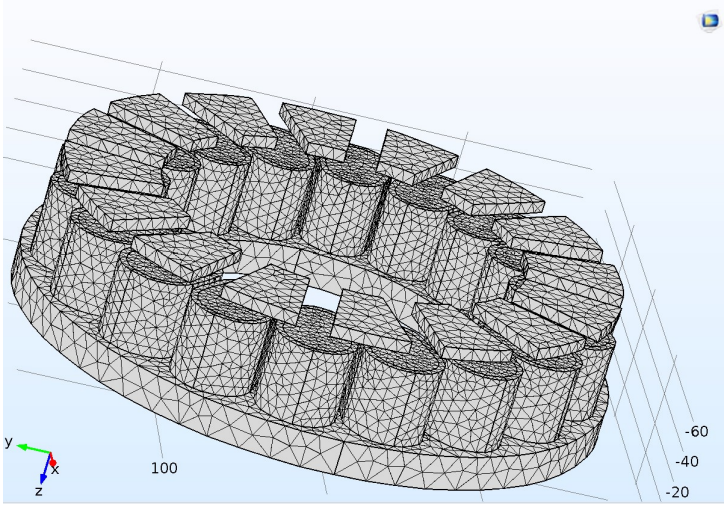

Figure 6.2: The final geometry meshed

6.2 Principles of modeling of electrical machines in 3D

The Rotating Machinery, Magnetic physical interface in COMSOL Multiphysics is designed specifically for modeling electric motors and generators. The geometry of the machine must comprehend both the stator and the rotor with an airgap that allows relative motion between the two. The geometry must be divided into two distinct objects, the division has to be done in the airgap in order to divide the stator from the rotor. Once the division between the stator and the rotor parts is done it is necessary to specify which part belongs to the stator and which to the rotor using the **form union** feature. Form union is the default geometry finalization method used by Comsol, it is equivalent to apply a Boolean union to the selected parts of the geometry, this allows to define a single **object** made by different **domains**. By definitions the form union function does not allow relative motion between the domains of a same object. Once the stator and the rotor are defined as two separate object it is necessary to define the boundary between them, to do so the **form assembly** feature is applied. Form assembly identifies the touching, adjacent, boundaries of all objects and by default it forms the so-called **Identity Pairs**. By default, there is no continuity of the fields or the fluxes across a boundary Pair. Continuity at pair boundaries must be explicitly applied. The form assembly feature also allows to mesh the stator and the rotor parts separately, this allows to impose a **moving mesh** type to the rotor to simulate the motion. Moreover the geometry defined in section 6.1

must be inserted into an air environment simulated as a cylinder big enough to guarantee a consistent solution.

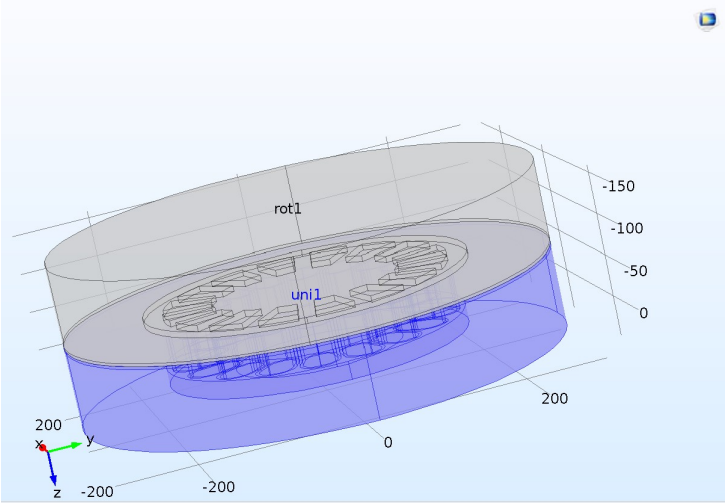

Figure 6.3: The stator part: Air (with air-gap), stator and windings

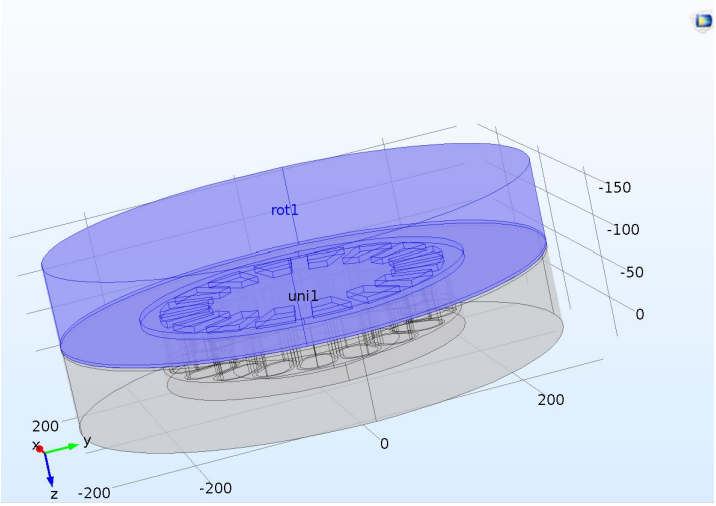

Figure 6.4: The rotor part: Air (with air-gap, rotor and magnets

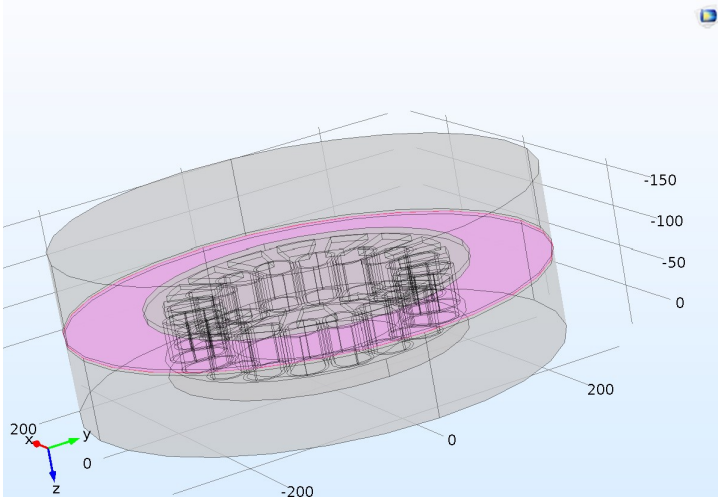

Figure 6.5: The identity pair between the stator and the rotor part

It is worth noting that the geometry used in the simulations has only one stator while the designed motor has two of them, this has been done to make the simulation lighter. Once the values of back emf and torque have been deduced from the simulations, their values have to be doubled to take into account the second stator. This simple procedure is accurate since the two stators are aligned symmetrically with respect to the rotor.

6.2.1 The mixed formulation

The Maxwell's equations can be solved with two approaches. One approach is to use the **vector magnetic potential** $\vec{A}$, in this case the electric field and the magnetic field are expressed as:

$$\vec{E} = -\frac{\partial \vec{A}}{\partial t} \tag{6.1}$$

$$\vec{B} = \nabla \times \vec{A} \tag{6.2}$$

Thanks to this formulation, Faraday's law 2.3 and magnetic flux conservation law 2.6 are automatically fulfilled.

The equation to be solved is the Apere's law (equation 2.4). Thanks to the **quasistatic approximation** is possible to neglect the displacement current $\vec{D}$ and the equation becomes:

$$\nabla \times \vec{H} = \vec{J} \tag{6.3}$$

The other approach uses the **scalar magnetic potential** V_m. Here the magnetic field is described as the gradient of the potential. This approach is used when the current density $\vec{J}$ is zero, Ampère's law is automatically fulfilled and the magnetic flux conservation law is solved. This approach is less demanding in terms of computing power resulting in an easier problem to solve. When the two approaches are used together in the same model, they can be referred to as "mixed formulation".

It is worth to be noted that the scalar potential can only represent an irrotational magnetic field. In practice, there cannot be closed curves in the scalar potential region that completely enclose a current. To conclude, the vector potential method is the one to be used when there is current density in the domain under analysis. On the other hand the scalar potential method is strongly raccomanded where there are domains with no current density and helps to give robustness to the problem when it is applied in the domains adjacent to the identity pair boundary.

6.2.2 The coil analysis

COMSOL Multiphysics has a dedicated feature to numerically solve the motor coils physic called **coil geometry analysis**. The feature can solve coils of any geometry but it is strictly recommended to avoid coils with short edges. This study is mandatory when there are exited coils in the model.

There are two **types of coil features**, which differ from the physical system represented, the modeling details, and the applicability to a model:

- **Single-turn coil** models a single, solid region of a conducting material in which the current flows. It is recommended to use this feature to model a single wire with a non-negligible cross section.

- **Multi-turn coil** models a coil made by many wounded wires electrically insulated from each other. This feature allows to study the coil without modelling each single wire and it is recommended for the study of wounded motors such as in the case under exam.

When the Multi-turn coil feature is used, a **coil type** parameter is used to specify the geometry of the coil:

- **Linear**, in which the wires are straight and parallel

- **Circular**, in which the wires are wounded with a circular pattern around a common axis

- **Numeric**, in which the path of the wires in the coil is computed numerically in an additional study step during the solution. This allows the modeling of coils with complex shapes. The coil domain must be provided with an internal boundary in which the current flow direction has to be specified as can be seen in figure 6.6

The **excitement** can be imposed in two different ways:

- **Voltage**

  The coil is excited by imposign a desired voltage V_{coil}, both the amlpitude and the waveform can be chosen by the user.

- **Current**

  The coil is excited by imposing a desired current I_{coil}, both the amlpitude and the waveform can be chosen by the user. This modality is the most suitable when it is required to study the motor torque or the induced back-EMF. In the former the coil is excited with the nominal current, in the latter it is imposed a current of $0A$ in order to simulate the stator open circuit condition.

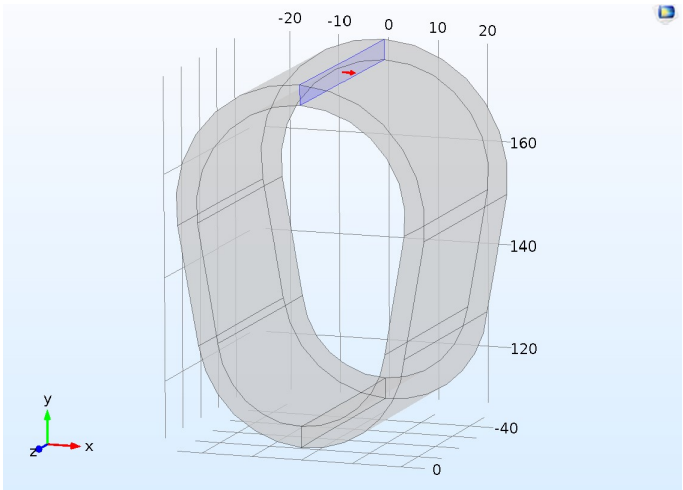

Figure 6.6: The model of the coil with the interior input boundary in evidence

The numerical computation of the coil has to be the first study step of the model as it is used as initial condition for the **stationary study step**.

6.3 Back EMF analysis

The aim of the simulation is to evaluate the peak value and the waveform of the back electromotive force produced in the motor because of the relative motion between the magnetic field of the permanent magnets and the stator windings, see also subsection 2.1.2. The peak value expected has to be around the 80% of the supply voltage peak witch is $V_{inverter} = 229V$. The waveform has to be as sinusoidal as possible to ensure an easy control of the machine. The simulation has been made imposing the phases as open circuits, this has been easily achieved by imposing $I_{coil} = 0[A]$. The angular velocity of the rotor for this test is the base velocity ω_b. The result showed in figure 6.7 represents the voltage induced in one phase of one stator of the motor, to obtain the total phase value (for both stators connected in series) the result has to be multiplied by two.

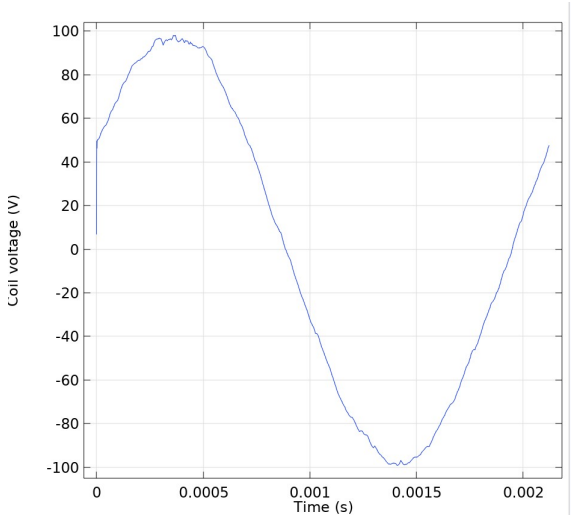

Figure 6.7: Results of the back emf simulation

The expected design peak value and the simulated one are reported and compared in the table below:

Project value	**Simulation result**	**Relative error**
$187V$	$194V$	3.7%

Table 6.1: Comparing back-emf results

since: $V_{inverter} = 229 > 194V$ the back-emf value is acceptable. The waveform has a huge first harmonic order, as expected.

6.4 Torque analysis

The aim of the simulation is to ensure that the motor is able to produce the desired torque of $T = 350Nm$ while rotating at his base speed ω_b. The simulation has been made imposing a continuous current in the first phase (phase A) of the motor which value is equal to the peak value of the nominal current of the motor $I_{a_{DC}} = \sqrt{2} * 330A$ and imposing the other two phases (B and C) as the closing path of the circuit so that $I_{b_{DC}} = I_{c_{DC}} = -I_{a_{DC}}/2$. Finally it has been studied the axial force acting on the magnets at different positions of the rotor and the results have been interpolated. The final position of the rotor has been chosen in order to simulate a rotation of at least two pole pitch, it is expected to encounter two points in which the torque is equal to $0Nm$ that correspond to the two d axis (one for each pole pitch) and two points of maximum torque corresponding to the q axis (see also appendix 9. The results give the maximum torque value for one stator, it is then necessary to multiply the result by two. The expected disegn value and the simulated one are reported and compared in the table below:

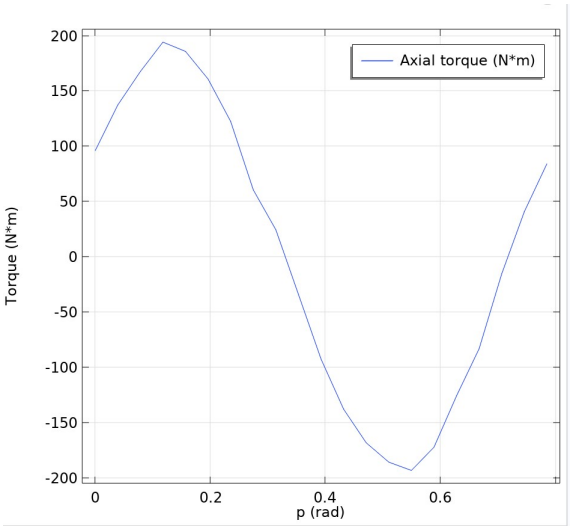

Figure 6.8: Result of the torque simulation

Project value	**Simulation result**	**Relative error**
$350Nm$	$380Nm$	8.5%

Table 6.2: Comparing torque results

The result of the simulation is coherent with what was expected since the relative error is less than 10%

6.5 Inductance analysis

In subsection 3.4.1 it has been said that the machine inductance can be modelled as the sum of two different components:

- The magnetizing inductance L_m
- The leakage inductance L_σ

The former parameter is easily deducible using the finite element software since is directly dependent on the nature of the coils. The leakage inductance is otherwise very difficult to evaluate correctly with the predefined features offered by the software. It is the personal view of the author that a further study on the software possibilities has to be done. For this work of thesisi only the magnetizing value of the inductance is evaluated both analytically and numerically. The value of L_m is deduced during the post processing of the simulation results applying the formula:

$$Lm = \frac{3}{2} L_{coil} \cdot m \tag{6.4}$$

where L_{coil} is the main inductance of one phase and m is the number of phases. The value of L_{coil} is deduced by dividing the concateneted flux of the phase coils with the current, these two value are given by the software automatically every time that a geometry coil analysis is used (see also 6.6).

$$L_{coil} = \frac{\Phi_{coil}}{I_{coil}} \tag{6.5}$$

The expected disegn value and the simulated one are reported and compared in the table below:

Project value	**Simulation result**	**Relative error**
$2.6 * 10^{-5} H$	$2.8 * 10^{-5} H$	7.6%

Table 6.3: Comparing main inductance results, the value is referred to a single stator

6.6 Losses and efficiency

In this section are reported the main procedures used to evaluate the motor efficiency numerically. The features given by the software have been found not well suiting this kind of problem, the losses are underestimated

and consequently the efficiency is overestimated. The reason of this issue and possible future solutions are also reported in this section.

The study of the losses has been divided into two different simulations, one for the Joule losses and the other for the iron ones.

6.6.1 Joule losses simulation

The Joule losses are calculated in the software by integrating the **volumetric loss density** variable with respect of all the domains that represents the coils in the model, selected in the figure below.

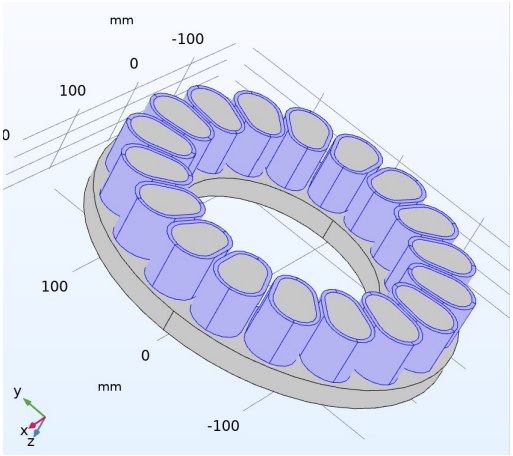

Figure 6.9: The coil domains in which the volumetric integral is applied

The volumetric loss density is automatically evaluate by the software everytime that a Coil geometry analysis study is used. This kind of procedure gives very accurate results in the case in which a stationary regime of current is used since there are no reactive effects such as skin effect and proximity effects that influence the total windings resistance (see also 4.1.2). The expected design value and the simulated one for a DC regime are reported and compared in the table below:

Project value	**Simulation result**	**Relative error**
$700W$	$640W$	8.57%

Table 6.4: Comparing total Joule losses results in a DC regime

On the other hand, when the coils are excited with a sinusoidal distribution of currents the AC effects that contribute to the resistance enhancement

are not considered by the software solution. The reasons can be of different natures:

- The **coil model** used for simulating the motor windings is the homogenized multi-turn coil (see 6.2.2) since it takes into account the number of windings and their cross section, however this model does not take into account the skin effect and the proximity effect properly. The reactive phenomena are better represented by the single-coil model but the information about the number of windings get lost and this means that a new dedicated cad model of the coils may be needed.
- **Poor meshing** in the coil region. As a matter of fact the region in which the skin effect is supposed to occur must present at least 10 mesh elements across the 90% of the skin depth region. This meshing condition is not always achievable since the model has a very high aspect ratio in the coil region.
- The **parallel conductors** in which is divided the wire of the coil is not a trivial task to modeling and so the real winding configuration showed in figure 4.2 is not replicable in the software model.

To estimate the Joule losses taking into account the AC effects it is proposed an hybrid model in which the DC effects P_{DC} are calculated by the mean of the FEA software and the AC effects,represented by the factor k_r, are added according to the model showed in subsection 4.1.2 and considering that:

$$P_{AC} = k_r P_{DC} \tag{6.6}$$

The losses have been calculated in five different operative points according to table 6.5 that refers to the flux weakening theory showed in appendix 9.

$\omega_m[rad/s]$	$i_d[A]$	$i_q[A]$	$i[A]$	$\alpha[deg]$
$370 = \omega_b$	0	466	$466 = \hat{I}_{max}$	0
465	$330 = \hat{I}_{ch}$	330	466	45
652	330	235	409	55
979	330	156	370	65
$4\omega_b$	330	105	351	72.5

Table 6.5: Different flux weakening operative point

As it can be seen the instantaneous value of phase current i decreases with the enhancement of the flux weakening angle α and this has to be taken into account when the losses are estimated. The results are reported in the table below:

$\omega_m[rad/s]$	$P_{DC}[W]$	k_e	$P_{AC}[kW]$
370	310.5	21	6.51
465	310.5	23.8	7.38
652	238.5	26.9	6.42
979	195.0	32.5	6.34
1480	175.6	39.5	6.93

Table 6.6: Hysteresis losses for five different operative points

6.6.2 Iron losses simulation

The iron losses are calculated in the software by integrating the **volumetric loss density** variable with respect of all the domains that represents the iron core in the model, selected in the figure below.

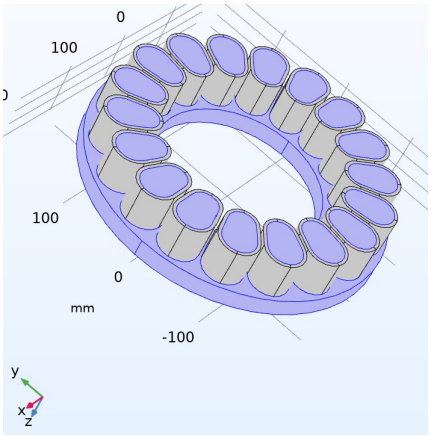

Figure 6.10: The iron domain in which the volumetric integral is applied

The volumetric loss density is automatically evaluated by the software everytime that an Ampere's law feature is used (see also 6.2). The simulation has been done by setting a time dependent study in which the coils, closely wounded around the core teeth are excited with a three phase sinusoidal distribution of current at the highest electrical frequency corresponding to the case in which the rotor is rotating at the maximum speed (flux weakening region). The motor has been designed to rotate up to four times the base speed, so:

$$f_{max} = \frac{4\omega_b pp}{2\pi} \tag{6.7}$$

The choice of studying the losses at the maximum frequency is due to the need to evaluate the worst case scenario since the iron loss has an increasing

trand with the supply frequency. During the simulation process two different issues have been detected:

- The analytical formula given by the manufacturer (and reported in section 4.3.2) to evaluate the specific losses in the SMC material is verified experimentally for a ring sample according to the normative CEI/IEC 60404-6:2003. The formula is not accurate anymore when applied to a more complex geometry such as the motor stator. For this reason a proper comparison between analitycal and numerical results is not possible. What has been said leads to the conclusion that the analytical and the numerical results can be compared only when a ring sample is used.

- The FEA software is capable of evaluating both eddy current and hysteresis losses. For the study of the hysteresis phenomena the software relies on the **Jiles-Atherton model** that requires some parameters that can only be deduced empirically and are not given by the material manufacturer. The missing parameters are reported in the table below:

Parameter name	**Measure unit**	**Symbol**
Domain wall density	$[A/m]$	a
Pinning losses	$[A/m]$	k_p
Magnetization reversibility	Adimensional	C_r
Inter-domain coupling	Adimensional	α

Table 6.7: Parameters required by the software to evaluate the hysteresis losses in the SMC material according to the Jiles-Atherton model

  What has been said leads to the conclusion that only the eddy current losses can be evaluated by the mean of the FEA software.

Considering the conclusions reported above, a **preliminary simulation** has been done with the aim of verify and compare the eddy current losses calculated both analytically and numerically. The simulation has been set modelling the ring sample described in normative CEI/IEC 60404-6:2003. The ring has been completely surrounded by a coil domain to give homogeneity to the magnetic flux through the material.

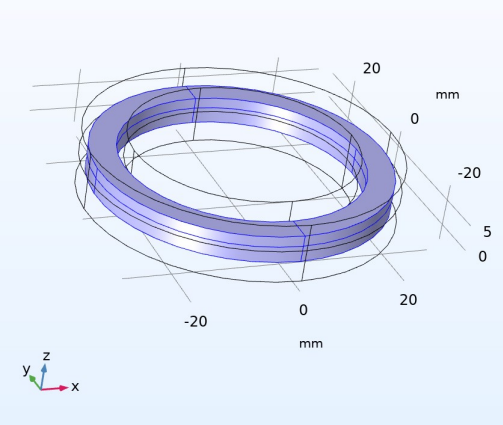

Figure 6.11: The model of the SMC ring (violet domain) surrounded by the excitement coil (transparent domain)

The setting data of the simulation are reported below:

Excitement data	**Value**	**Symbol**
Number of turns	90	N
Wire cross section	$9[mm^2]$	s_a
excitement current	$5[A]$	I
Current frequency	$2[kHz]$	f
Average magnetic flux density	$1.3[T]$	B_{avg}
Ring data		
Outer diameter	$55[mm]$	D_{out}
Inner diameter	$45[mm]$	D_{in}
Height	$5[mm]$	h
Ring volume	$1.57 \cdot 10^{-6}[m^3]$	V
Density	$7440[kg/m^3]$	ρ
Mass	$11 \cdot 10^{-3}[kg]$	m
Loss constants		
Eddy current constant	$1.4 \cdot 10^{-5}$	K_{ep}
Hysteresis constant	$7.9 \cdot 10^{-2}$	K_h

Table 6.8: Setting data for the ring sample test

According to equation 4.21 the eddy current specific losses in the ring sample can be evaluated analytically as:

$$p_{eddy} = K_{ep} f^2 B^2 \tag{6.8}$$

The analytical and numerical results are reported and compared below:

Analytical value	**Simulation result**	**Relative error**
$1[W]$	$0.9[W]$	10%

Table 6.9: Comparing eddy current losses results

As long as the relative error is under (or equal to) the 10% the FEA results can be considered reliable.

In order to estimate with a good approximation the losses in the core it has been decided to use an hybrid method in which the eddy current losses are deduced by the mean of the FEA software and the hysteresis losses are calculated analytically. The hysteresis losses in a ferromagnetic material go according to the formula

$$p_h = K_h f B^{1.75} \tag{6.9}$$

However the flux density B is not the same in all the stator so equation 6.9 cannot be applied directly, so it has been introduced the following function:

$$p_{diff}(f) = p_h(f) - p_{eddy}(f) \tag{6.10}$$

$P_{diff}(f)$ is defined as the difference between the hysteresis specific losses and the eddy current specific losses in the ferromagnetic material for a given flux density distribution and depends on the frequency. For hypotesis $P_{diff}(f)$ has been assumed to be always the same for a given frequency, thus the difference between eddy current losses and hysteresis ones has been considered as not dependant on the iron geometry.

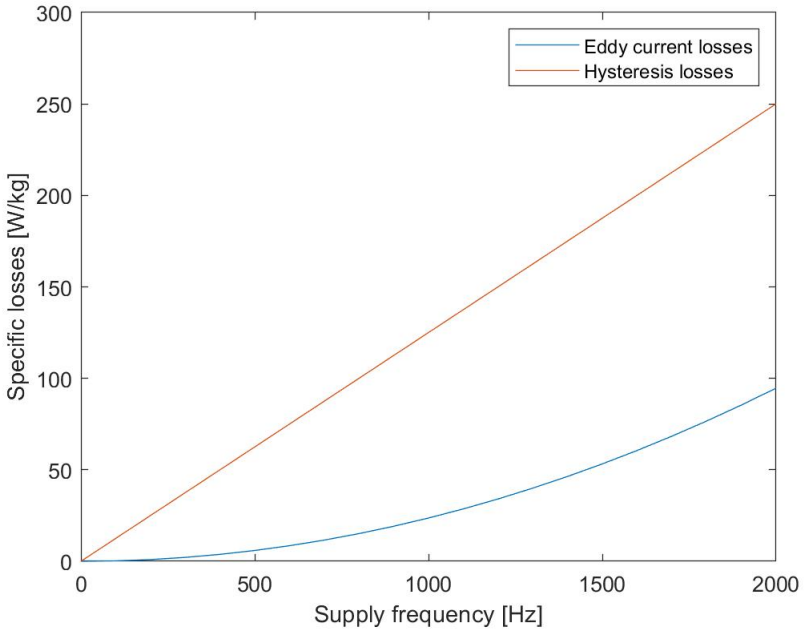

Figure 6.12: Iron specific losses trend for different supply frequency values at $1.3T$

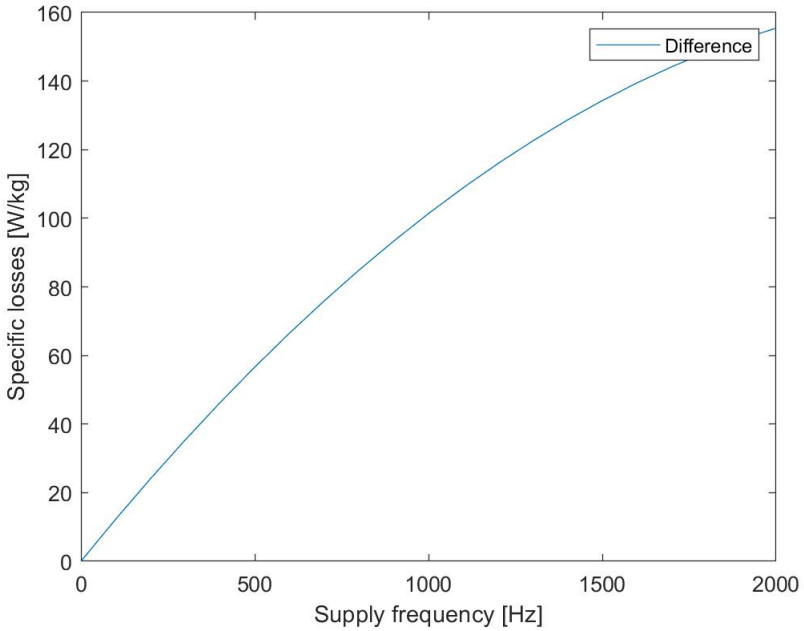

Figure 6.13: The trend of the function $p_{diff}(f)$ at $1.3T$

Moreover it is necessary to take in account the fact that during the flux weakening of the machine the module of the armature current is reduced and this has a direct effect on the module of the magnetic flux density in the core. According to the appendix 9, are reported in table 6.5 the currents and the rotational speed for some operative points of the machine. In order to consider all the operative points in table 6.5, the function $p_{dif}(f)$ has been calculated for different values of flux density as shown in figure

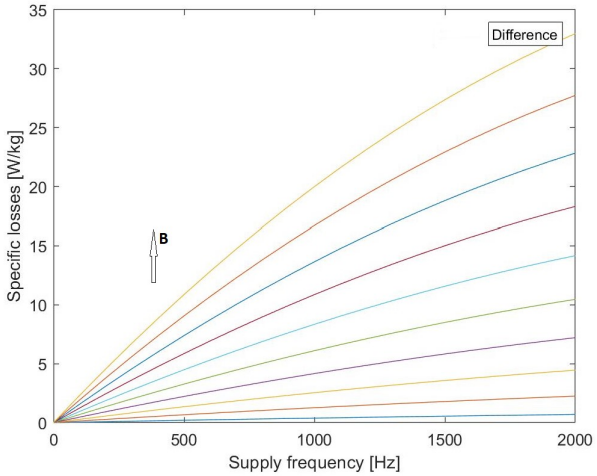

Figure 6.14: The function $p_{dif}(f)$ from $B = 0.05T$ to $B = 0.5T$ with an increment of $0.05T$

Finally, for each operative point in table 6.5 an eddy current losses simulation has been done on the stator core model and to obtain the hysteresis losses the following formula has been used:

$$P_h = P_{eddy} + p_{diff} \cdot m_{iron} \tag{6.11}$$

Where m_{iron} is the iron mass of the stator. In table 6.10 are reported the iron losses results.

Where P_{tot} is the sum of eddy current losses and hysteresis losses multiplied by two to take into account the presence of two stators.

6.6.3 Efficiency

Considering that the motor has a nominal power of $P_{motor} = 130[kW]$, the efficiency is calculated as:

$$\frac{P_{motor} - P_{tot}}{P_{motor}} \cdot 100 \tag{6.12}$$

$\omega_m[rad/s]$	$P_{eddy}[W]$	$P_h[W]$	$P_{iron}[W]$
370	7	56	126
465	10.5	71.6	164
652	16	98.9	229.8
979	29	146.5	351
1480	60	222.15	564.3

Table 6.10: Hysteresis losses for five different operative points

In table 6.11 is reported the efficiency for the five operative points analyzed in subsection 6.6.1 and 6.6.2.

$\omega_m[rad/s]$	$P_{Joule}[kW]$	$P_{iron}[kW]$	$P_{tot}[W]$	μ
370	6.51	0.13	6.64	94.89%
465	7.38	0.16	7.54	94.20%
652	6.42	0.23	6.65	94.88%
979	6.34	0.35	6.69	94.85%
1480	6.93	0.56	7.49	94.23%

Table 6.11: Hysteresis losses for five different operative points

6.7 Rotor mechanical analysis

Since the rotor in an axial configuration SRS is very thin, $7.6mm$ in the case under exam, and it is supposed to rotate at $\omega_{max} = 1480[rad/s]$, which is a relatively high velocity, it is appropriate to study the centrifugal stress and the periferical fibers displacement. To do so a finite element analysis has been performed simulating the rotor in a uniform rotating motion with rotational speed equal to v_{max}. The displacement is more than acceptable with a maximum value of $9.5 * 10^{-4}mm$. The simulation also confirms that the maximum tensile strenght of the material is not reached in any point of the rotor.

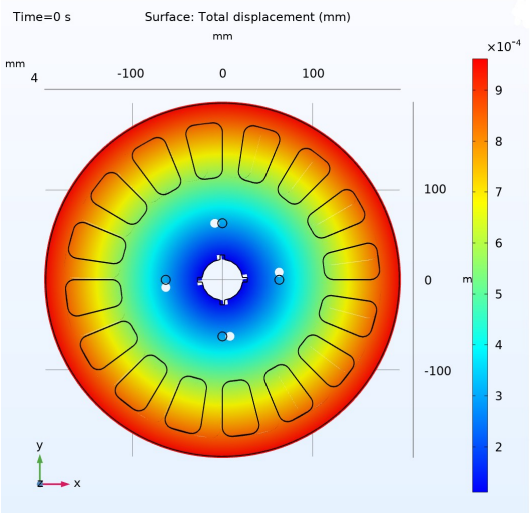

Figure 6.15: Displacement of the fiber of the disk at $1480 rad/s$

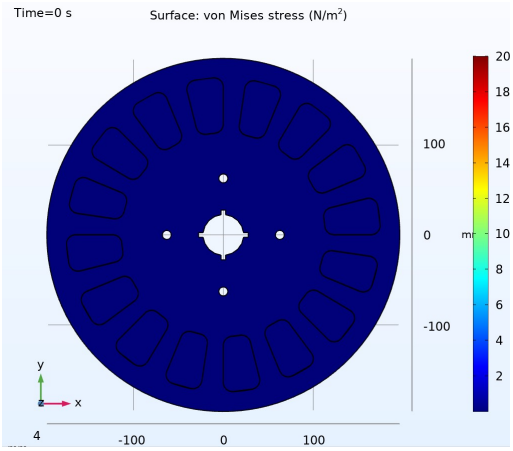

Figure 6.16: Von Mises stress in the disk at $1480 rad/s$

Chapter 7

Final motor layout and constructive choices

In this chapter it is reported the final motor layout and the constructive choices adopted.

7.1 Motor layout and mechanical choices

7.1.1 External layout

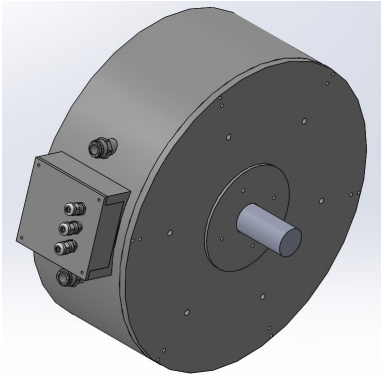

Figure 7.1: 3D model of the motor (front)

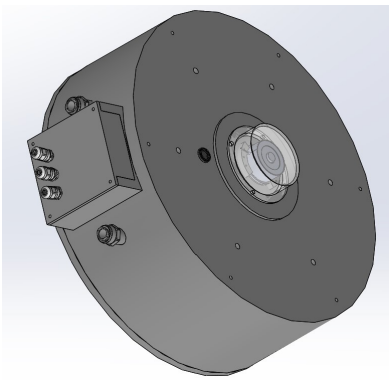

Figure 7.2: 3D model of the motor (back)

Externally the motor presents on one side the shaft and on the other the resolver which has been placed outside the motor for both constructive reasons and EMC reasons. On the same side of the resolver it is placed the signal connector (24 pin) which is used as output for the temperature sensors and the resolver as well. The inlet and outlet of the cooling jacket are placed in the proximity of the power connections in order to have the widest surface of heat exchange possible.

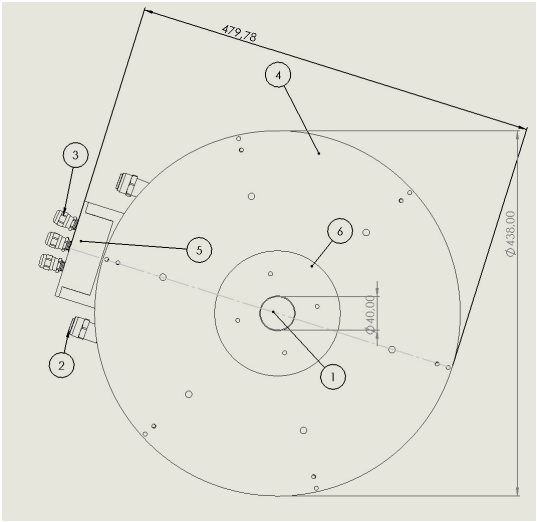

Figure 7.3: Exterior parts (front)

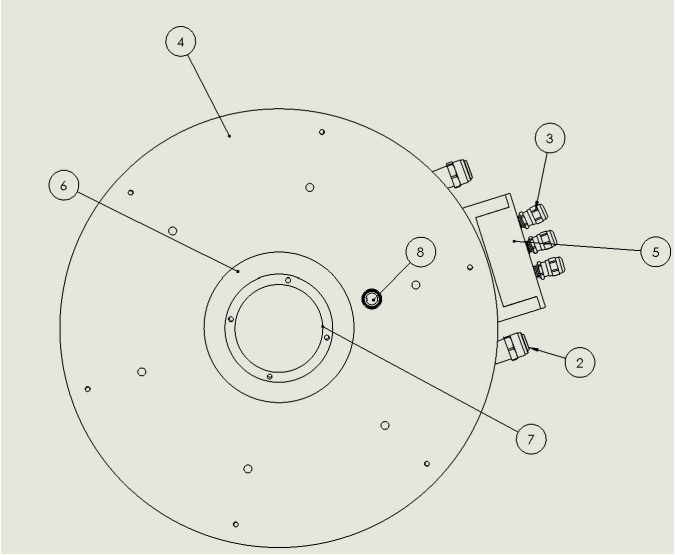

Figure 7.4: Exterior parts (back)

1. Shaft
2. Cooling inlet/outlet
3. Phase outer connection
4. Motor case
5. Phase inner connection case
6. Outer bearing constraint
7. Resolver
8. M24 signal connector

7.1.2 phase inner connection case

The motor designed has two stators connected in series. The series connection is done insied the phase inner connection case thanks to a simple system of screw, cable lugs and copper busbar:

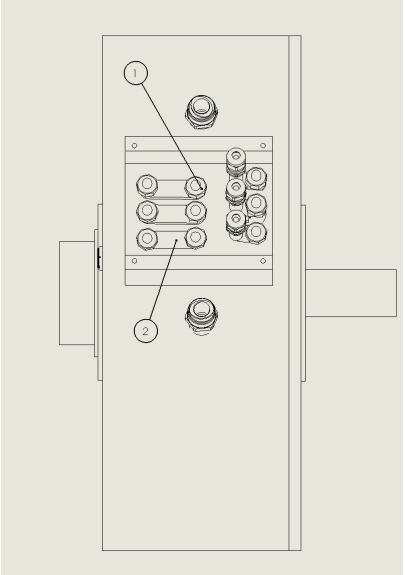

Figure 7.5: Phase inside connection case (upper)

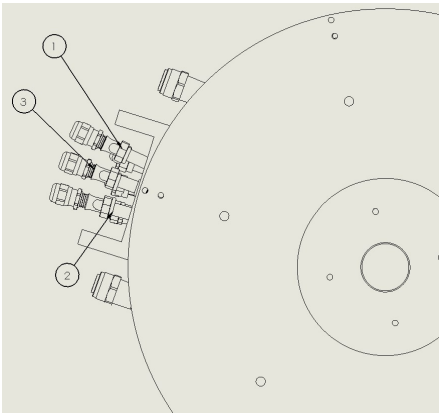

Figure 7.6: Phase inside connection case (upper view)

1. Screw
2. Copper Busbar
3. Cable lug

7.1.3 Inner parts

Inside the case the motor is surrounded by the cooling jacket in which the water flows through seven channels. The rotor and the shaft are constrained

by the mean of a lock nut and locking washer (for more details about the constrains between the rotor and the shaft see 7.1.4). The contact between the case and the shaft is mediated by two bearings (one on every side of the motor).

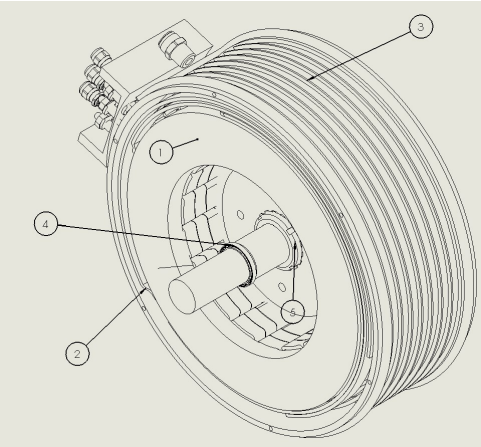

Figure 7.7: Inner motor parts (lateral view)

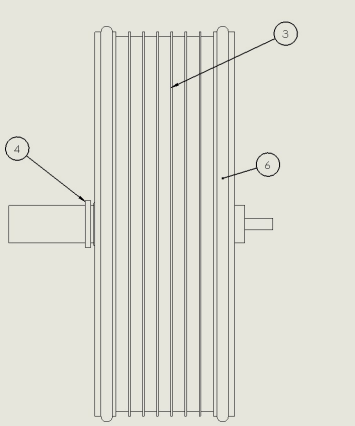

Figure 7.8: Inner motor parts (upper view)

1. Stator
2. Coil
3. Cooling jacket
4. Bearing

5. Lock nut and locking washer

6. O-ring

7.1.4 Rotor and shaft

The shaft is inserted into the rotor and denies the shifting of the rotor in one of the two axial directions thaks to its variable diameter, as a matter of fact the biggest radial dimension of the shaft is bigger than the rotor central hole. On the other side of the rotor the axial movement is constrained by the mean of a lock nut and locking washer (see fig.7.7). The torque produced by the magnets is transfered to the shaft by the means of keys. The thinnest part of the shaft is the one in which the resolver is installed.

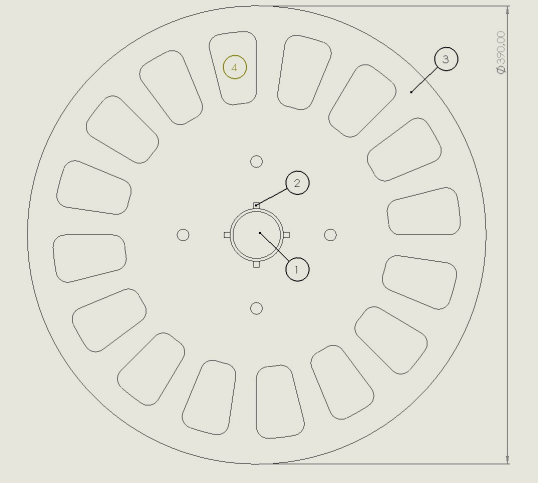

Figure 7.9: The shaft and the rotor (front view)

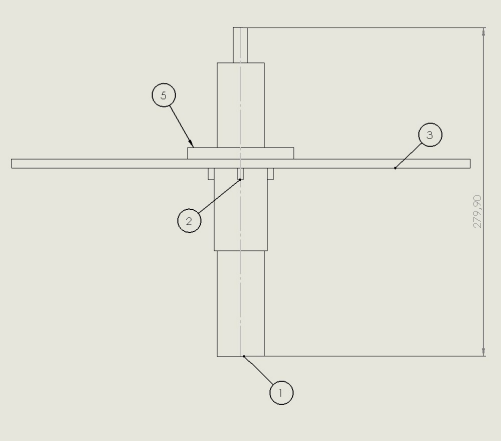

Figure 7.10: The shaft and the rotor (lateral view)

1. Shaft

2. Key

3. Rotor

4. Magnet NdFeB

5. Part of the shaft with the largest diameter

7.1.5 Exploded view

For a better comprehension of the motor design, here is reported an exploded view.

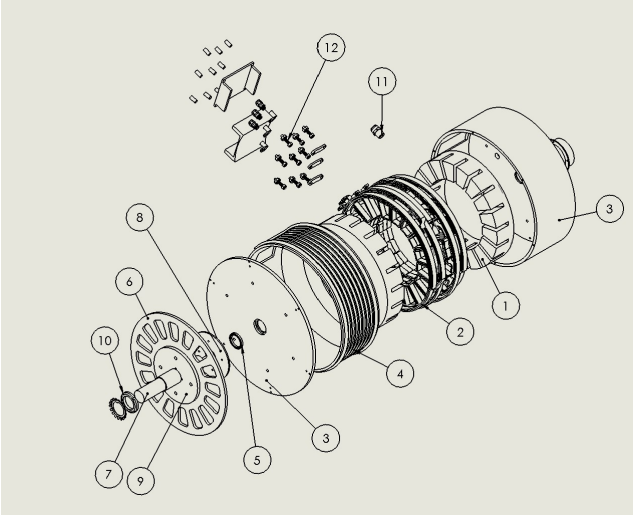

Figure 7.11: Exploded motor

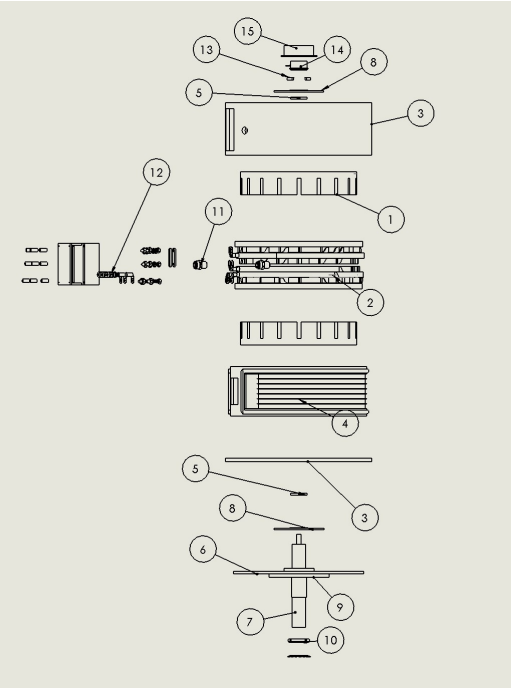

Figure 7.12: Exploded motor (upper view)

1. Stator

2. Windings

3. Outer case
4. Cooling jacket
5. Bearings
6. Rotor
7. Shaft
8. Bearing constraint
9. Additional rotor constraint
10. Lock nut and locking washer
11. Inlet/outlet cooling jacket
12. Electrical connections
13. Resolver constraint
14. Resolver
15. Resolver case

7.2 Sensors

The motor is equipped with position and temperature sensors for control and diagnostic reasons.

7.2.1 Position sensor

The TEconnectivity 2360964-1 has been chosen as position sensor. Here are reported the main device parameters:

2360964-1	**Data name**	**Value**
Mechanical parameters	Size	$21[mm]$
	Shaft inner diameter	$12.7[mm]$
	Pole pairs	1
	Max. rotational speed	$20000[rpm]$
Electrical parameters $(22°C)$	input voltage	$5V$
	Frequency typical	$4[kHz]$

Table 7.1: Resolver main parameters

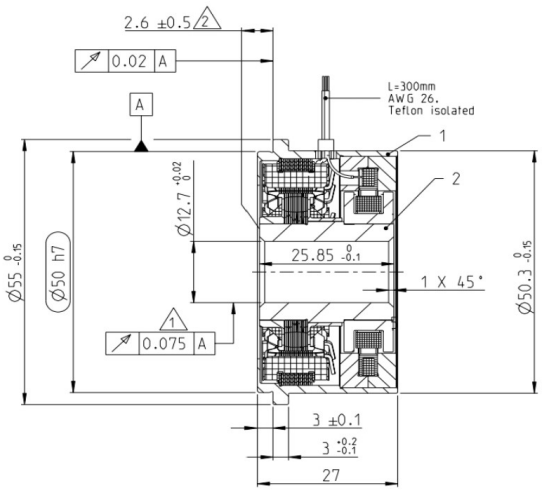

Figure 7.13: Resolver, tranversal section

7.2.2 Temperature sensor

An electric motor usually has one temperature sensor that is positioned exactly in the point in which the motor tends to present the highest temperature during his normal functioning. Since this "hot spot" is not known but has to be found empirically ad since the motor designed is a prototype, it is a good practice to use how many temperature sensors as possible. For the prototype designed at least two sensor needs to be used, one per stator. As a temperature sensor it is uses a **cable sensor in ceramic sleeve** made by Ephy Mess. The sensors are directly inserted in the head windings of the machine.

Chapter 8

Conclusions

The finite element analysis confirms the values of the project design. The motor prototype designed is industrially buildable and easily applicable to a power train environment. Future studies need to be done for a proper thermal characterization of the machine in every working point. A further finite element study on the d and q axes inductance in function of the axes currents needs to be done to characterize the cross saturation effects and to produce a flux map in order to be able to control properly the motor. The finite element study on the cross saturation may be used also as a sensitivity analysis to identify the minimum back iron thickness that minimizes the iron volume without invalidating the torque production. The overall results are satisfactory and the design procedure used in this work of thesis can be reused for the design of radial flux PM motors as well

Chapter 9

Appendix: Control of a brushless motor with sinusoidal back EMF

9.1 Torque in a brushless motor with sinusoidal back EMF

9.1.1 Matrix notation

Given a three-phase motor and assuming that every phase has equal electrical characteristics. The star point **N** is virtually put outside the motor in order to be able to measure the star voltage of each phase and, for a generic phase named n, it can be expressed as:

$$v_{nN} = R \cdot i_n + \frac{d\lambda_n}{dt} \tag{7.1}$$

Where:

- v_n is the **instantaneous** voltage value between the star point N and the phase supply point n
- i_n is the **instantaneous** current value flowing in the phase n
- R is the phase resistance, equal for each phase
- λ is the magnetic flux concatenated with the phase n and it is equal to

$$\lambda_n = \lambda_{mn} + L_{eq} \cdot i_n \tag{7.2}$$

where L_{eq} is the equivalent inductance of the phase that take into account both the auto and mutual effects and λ_{mn} is the magnetic flux concatenated with the phase n generated by the permanent magnets.

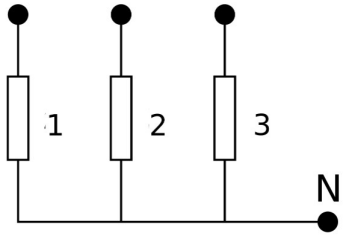

Figure 9.1: Motor phaeses configuration

When using equation 7.1 to refer to each of the three motor phases is wise to use a matrix notation:

$$\begin{bmatrix} v_{1N} \\ v_{2N} \\ v_{3N} \end{bmatrix} = R \begin{bmatrix} i_1 \\ i_2 \\ i_3 \end{bmatrix} + \begin{bmatrix} \frac{d\lambda_1}{dt} \\ \frac{d\lambda_2}{dt} \\ \frac{d\lambda_3}{dt} \end{bmatrix} \tag{7.2}$$

That can be summarized in:

$$\bar{v} = R\bar{i} + \frac{d}{dt}\bar{\lambda} \tag{7.4}$$

9.1.2 Energy balance

The instantaneous torque produced by the motor can be desumed by the mean of an energy balance as follows:

$$\bar{p} = \bar{i}^t\bar{v} = \bar{i}^t R\bar{i} + \bar{i}^t L_{eq}\frac{d\bar{i}}{dt} + \bar{i}^t\bar{e} \tag{7.5}$$

where:

$$\bar{p} = \begin{bmatrix} p_1 \\ p_2 \\ p_3 \end{bmatrix} \tag{7.6}$$

is the vector of the instantaneous power of the three phases.

$$\bar{e} = \begin{bmatrix} e_1 \\ e_2 \\ e_3 \end{bmatrix} = \begin{bmatrix} \frac{d\lambda_{m1}}{dt} \\ \frac{d\lambda_{m2}}{dt} \\ \frac{d\lambda_{m3}}{dt} \end{bmatrix} \tag{7.7}$$

is the vector of the phases back-emf

Equation 7.5 shows three different components of the instantaneous power, respectively: The vector $\bar{p_j}$ of the phase instantaneous joule losses can be expressed as

$$\bar{p_j} = \bar{i}^t R \bar{i} \tag{7.8}$$

The vector $\bar{p_m}$ of the instantaneous variation of the magnetic energy can be expressed as

$$\bar{p_m} = \bar{i}^t L_{eq} \frac{d\bar{i}}{dt} \tag{7.9}$$

Finally the vector $\bar{p_\omega}$ of the instantaneous mechanical power can be expressed as follows, considering that the concatenated permanent magnet flux is a function of the position of the rotor $\theta_m(t)$ which is a function of time.

$$\bar{p_\omega} = \bar{i}^t \bar{e} = \bar{i}^t \frac{d\bar{\lambda_m}}{dt} = \bar{i}^t \frac{d\bar{\lambda_m}}{d\theta_m} pp \cdot \omega_m \tag{7.10}$$

Where the derivative of θ_m with respect of time is the mechanical rotor speed ω_m in $[rad/s]$. From equation 7.10 is possible to deduce the istantaneous torque produced by the motor:

$$T = \bar{i}^t \frac{d\bar{\lambda_m}}{d\theta_m} pp \tag{7.11}$$

9.2 Clarke transformation

A three-phase coil system can be graphically represented in a Gauss plane as three **spatial vectors** equally spaced of 120°and with amplitude N which is the number of turns of the coil. The direction of the three vectors is given by the triad of versors $\{\hat{n_1}, \hat{n_2}; \hat{n_3}\}$.

$$\begin{cases} \bar{N_1} = N \times \hat{n_1} = N \cdot (cos(\alpha_1) + jsin(\alpha_1)) = Ne^{j0} \\ \bar{N_2} = N \times \hat{n_2} = N \cdot (cos(\alpha_2) + jsin(\alpha_2)) = Ne^{j\frac{2\pi}{3}} \\ \bar{N_3} = N \times \hat{n_3} = N \cdot (cos(\alpha_3) + jsin(\alpha_3)) = Ne^{j\frac{4\pi}{3}} \\ \end{cases} \tag{7.12}$$

where the generic α_k is the phase of the spatial spatial vector k and is equal to:

$$\alpha_k = (k-1) \cdot \frac{2\pi}{3} \tag{7.13}$$

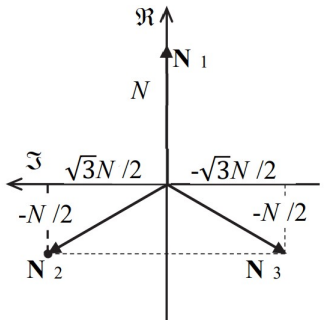

Figure 9.2: Coil spatial vectors of a three-phase system

Once the coil axis are defined is possible to define a spacial current vector I_{max} whose projections on the three axis represents the istantaneus value of the corresponding coil currents $\{i_1, i_2; i_3\}$. In the hipotesis of sinusoidal currents:

$$\begin{cases} i_1 = \mid I_{max} \mid cos(\theta) \\ i_2 = \mid I_{max} \mid cos(\theta - \frac{2\pi}{3}) \\ i_3 = \mid I_{max} \mid cos(\theta - \frac{4\pi}{3}) \end{cases} \tag{7.14}$$

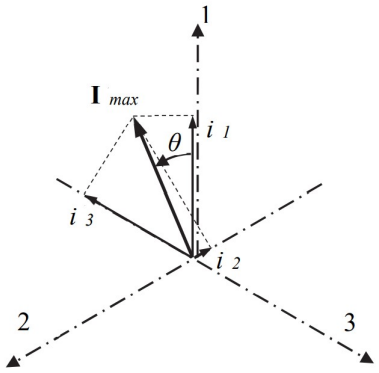

Figure 9.3: The spatial current vector

It is now possible to simplify the notation by the mean of a coordinate transformation, called the Clarke transformation, that allows to study the three-phase machine as a two phase equivalent one no more described by the triplet $\{\hat{n_1}, \hat{n_2}; \hat{n_3}\}$ but by two orthogonal axis $\{\hat{a}, \hat{b}\}$. The Clarke coordinate transformations are:

$$\begin{cases} \hat{n_1} = \hat{a} \\ \hat{n_2} = -\frac{1}{2}\hat{a} + \frac{\sqrt{3}}{2}\hat{b} \\ \hat{n_3} = -\frac{1}{2}\hat{a} - \frac{\sqrt{3}}{2}\hat{b} \end{cases} \tag{7.15}$$

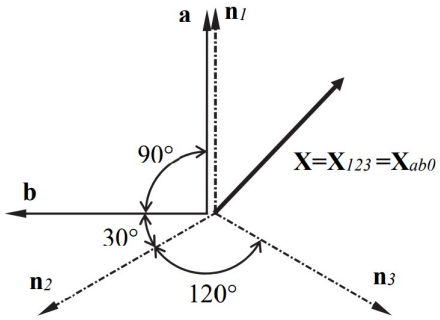

Figure 9.4: Clarke transformation for a given spatial vector X

So the relation between the current triad and the new current couple is:

$$\begin{bmatrix} i_1 \\ i_2 \\ i_3 \end{bmatrix} = \begin{bmatrix} 1 & 0 \\ -\frac{1}{2} & \frac{\sqrt{3}}{2} \\ -\frac{1}{2} & -\frac{\sqrt{3}}{2} \end{bmatrix} \begin{bmatrix} i_a \\ i_b \end{bmatrix} = \bar{C_{an}} \begin{bmatrix} i_a \\ i_b \end{bmatrix} \tag{7.16}$$

The inverse relation is:

$$\begin{bmatrix} i_a \\ i_b \end{bmatrix} = \begin{bmatrix} \frac{2}{3} & -\frac{1}{3} & -\frac{1}{3} \\ 0 & \frac{1}{\sqrt{3}} & -\frac{1}{\sqrt{3}} \end{bmatrix} \begin{bmatrix} i_1 \\ i_2 \\ i_3 \end{bmatrix} = \bar{C_{na}} \begin{bmatrix} i_1 \\ i_2 \\ i_3 \end{bmatrix} \tag{7.17}$$

9.3 Park transformation

Sometimes can be useful to refer the electric and magnetic quantities of the machine with respect to a system of axis that rotates with respect to the physical axis described by the versors $\{\hat{a}; \hat{b}\}$, whereas the rotating system is identified by the new couple of versors $\{\hat{d}; \hat{q}\}$. Referring to figure 9.5 it is easily deducible that :

$$\begin{cases} \hat{d} = \hat{a}cos(\theta) + \hat{b}sin(\theta) \\ \hat{q} = -\hat{a}sin(\theta) + \hat{b}cos(\theta) \end{cases} \tag{7.18}$$

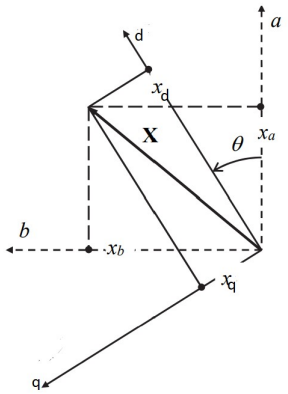

Figure 9.5: Park transformation for a given spatial vector X

So the relation between the currents in the old fixed system and the ones in the new moving one is:

$$\begin{bmatrix} i_d \\ i_q \end{bmatrix} = \begin{bmatrix} cos(\theta) & sin(\theta) \\ -sin(\theta) & cos(\theta) \end{bmatrix} \begin{bmatrix} i_a \\ i_b \end{bmatrix} = \bar{A}(\theta) \begin{bmatrix} i_a \\ i_b \end{bmatrix} \tag{7.19}$$

The inverse relation is:

$$\begin{bmatrix} i_a \\ i_b \end{bmatrix} = \begin{bmatrix} cos(\theta) & -sin(\theta) \\ sin(\theta) & cos(\theta) \end{bmatrix} \begin{bmatrix} i_d \\ i_q \end{bmatrix} = \bar{A}^{-1}(\theta) \begin{bmatrix} i_d \\ i_q \end{bmatrix} \tag{7.20}$$

The operator $\bar{A}(\theta)$ can also be expressed with the **complex notation** as follows:

$$\bar{A}(\theta) = e^{j\theta} \tag{7.21}$$

9.4 Brushless motor in the dq axes

By imposing the dq axes fixed with the rotor and by orienting the d axis in the direction in which the module of magnetic flux of the permanent magnet is higher (see figure 9.7) it is possible to apply the transformations introduced in section 9.3 and section 9.2 to simplify equation 7.2 as follow:

$$\bar{C_{na}} \begin{bmatrix} v_{1N} \\ v_{2N} \\ v_{3N} \end{bmatrix} = R \cdot \bar{C_{na}} \begin{bmatrix} i_1 \\ i_2 \\ i_3 \end{bmatrix} + \bar{C_{na}} \begin{bmatrix} \frac{d\lambda_1}{dt} \\ \frac{d\lambda_2}{dt} \\ \frac{d\lambda_3}{dt} \end{bmatrix} = \begin{bmatrix} v_a \\ v_b \end{bmatrix} = R \begin{bmatrix} i_a \\ i_b \end{bmatrix} + \begin{bmatrix} \frac{d\lambda_a}{dt} \\ \frac{d\lambda_b}{dt} \end{bmatrix} \tag{7.22}$$

and than:

$$e^{j\theta}\begin{bmatrix} v_a \\ v_b \end{bmatrix} = e^{j\theta} R \begin{bmatrix} i_a \\ i_b \end{bmatrix} + \begin{bmatrix} \frac{d\lambda_a e^{j\theta}}{dt} \\ \frac{d\lambda_b e^{j\theta}}{dt} \end{bmatrix} = \begin{bmatrix} v_d \\ v_q \end{bmatrix} = R \begin{bmatrix} i_d \\ i_q \end{bmatrix} + j\omega \begin{bmatrix} \lambda_d \\ \lambda_q \end{bmatrix} + \begin{bmatrix} \frac{d\lambda_d}{dt} \\ \frac{d\lambda_q}{dt} \end{bmatrix} \quad (7.23)$$

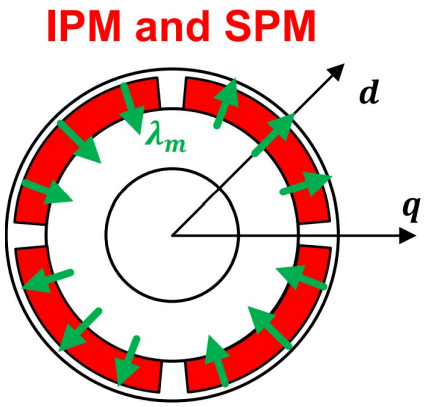

Figure 9.6: The d and q axises disposition with respect to the motor

The new system of equation that describes the equivalent machine in the dq system is:

$$\begin{cases} \begin{bmatrix} v_d \\ v_q \end{bmatrix} = R \begin{bmatrix} i_d \\ i_q \end{bmatrix} + j\omega \begin{bmatrix} \lambda_d \\ \lambda_q \end{bmatrix} + \begin{bmatrix} \frac{d\lambda_d}{dt} \\ \frac{d\lambda_q}{dt} \end{bmatrix} \\ \begin{bmatrix} \lambda_d \\ \lambda_q \end{bmatrix} = \begin{bmatrix} L_d & 0 \\ 0 & L_q \end{bmatrix} \begin{bmatrix} i_d \\ i_q \end{bmatrix} + \begin{bmatrix} \lambda_m \\ 0 \end{bmatrix} \end{cases} \quad (7.24)$$

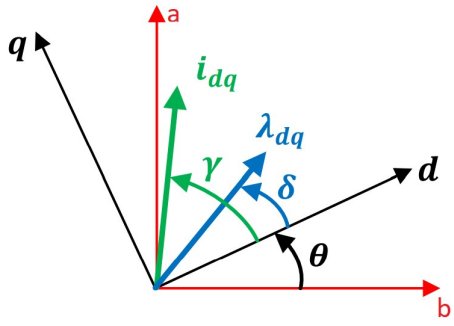

Figure 9.7: The vectors of current and flux reported in the dq system

Since the motor is isotropic:

$$L_d = L_q = L_{eq} \tag{7.25}$$

The torque expression found in section 9.1 can be reported in the new dq system as well:

$$T = \frac{3}{2} p(\lambda_m i_q) \tag{7.26}$$

9.5 Flux weakeing

9.5.1 Overall view over the flux weakening technique

According to figure 9.8 the operative region of the motor in function of the rotation velocity ω can be divided in two distinct intervals:

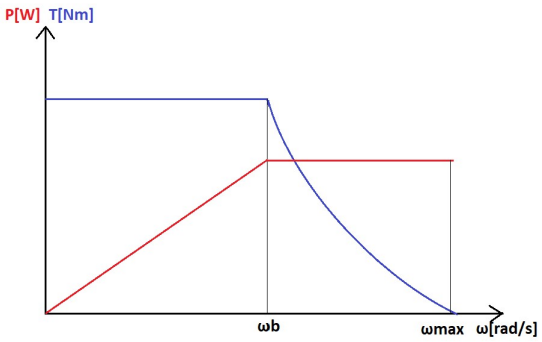

Figure 9.8: Power and torque in function of the rotational velocity of the motor

- $0 < \omega < \omega_b$

  Equation 7.26 shows that, in the dq system, only the current component in the q axis contributes to the torque production. Thus, up to the base speed w_b, the motor is controlled imposing the current distribution described in figure 9.10.

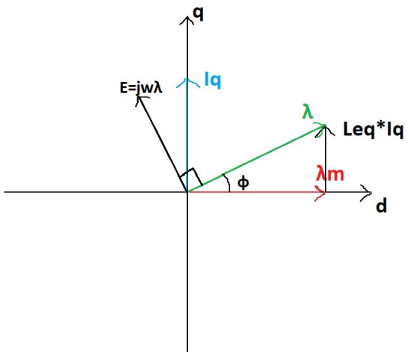

Figure 9.9: Main electrical and magnetical quantities of the motor for a maximum torque output

$$\begin{cases} i_d = 0[A] \\ i_q = I_{max} \end{cases} \tag{7.27}$$

It is worth noting that in this operative condition the power factor of the machine is easily deducible as follows:

$$cos(\phi) = cos(tg^{-1}(\frac{L_{eq} i_q}{\lambda_m})) \tag{7.28}$$

- $\omega_b < \omega < \omega_{max}$

  When the motor reaches the base speed ω_b, the back emf (which is proportional to the speed) equals the supply voltage and this means that it is no longer possible to increase the speed further while maintaining the current distribution described in 7.27. To reach the maximum speed of the motor is necessary to use the **flux weakening** technique in which a proper distribution of currents is used to induce a magnetic flux in the airgap that is in opposition with the flux of the permanent magnets. A fundamental parameter for the flux weakening is the **short circuit current** I_{ch}:

$$I_{ch} = \frac{\lambda_{pm}}{L_{eq}} \tag{7.29}$$

  The short circuit current represents the module of the current necessary to oppose completely to the permanent magnets magnetic flux. The flux weakening technique is well described in figure

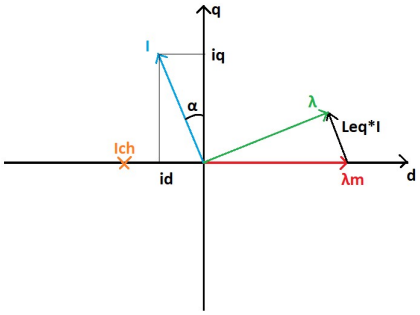

Figure 9.10: Flux weakening by shifting the current vector by an angle α

The new current distribution can be expressed as:

$$\begin{cases} i_d = I_{max} sin(\alpha) \\ i_q = I_{max} cos(\alpha) \end{cases} \tag{7.30}$$

If $I_{max} > I_{ch}$ then exist a value of $\alpha = \alpha_{ch}$ for which results $i_d = I_{ch}$, at this point the maximum torque available can be achieved with the minimum module of current by increasing further the angle α while maintaining the value of $i_d = I_{ch}$ as showed in figure 9.11.

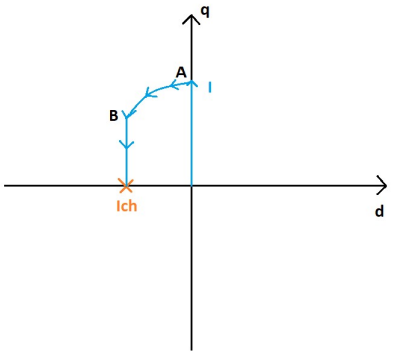

Figure 9.11: Position of the current vector during the flux weakening

It is possible to identify two different moments in the field weakening procedure here indicated as A and B. From point A to point B the current distribution follows the function 7.30. From point B the component in the d axis is always $i_d = I_{ch}$.

9.5.2 Speed computation in the flux weakening region

In this subsection is suggested a mathematical model to evaluate the rotor speed in function of the current vector shift. Using the complex notation it is possible to say that:

$$\lambda = \lambda_m + L_{eq} i_d + j L_{eq} i_q \tag{7.31}$$

Introducing $i = \sqrt{i_d^2 + i_q^2}$ Now the module of the flux can be expressed as follows:

$$\mid \lambda \mid^2 = \mid (\lambda_m - i L_{eq} sin(\alpha) + j(i L_{eq} cos(\alpha)) \mid^2 = \lambda_m^2 (1 - 2\frac{i L_{eq}}{\lambda_m} sin(\alpha) + \frac{i^2 L_{eq}^2}{\lambda_m}) \tag{7.32}$$

Introducing the notation:

$$A = \frac{L_{eq} i}{\lambda_m} \tag{7.33}$$

$$\mid \lambda \mid = \lambda_m \sqrt{1 - 2A sin(\alpha) + A^2} \tag{7.34}$$

When the motor is supplied with the maximum inverter voltage V, the mechanical speed is expressed as the ratio:

$$\omega_m = \frac{V}{\lambda pp} = \frac{V}{\lambda_m \sqrt{1 - 2A sin(\alpha) + A^2} pp} \tag{7.35}$$

Chapter 10

Bibliography

[1] Kartik Sitapati, R. Krishnan, "*Performance Comparisons of Radial and Axial Field, Permanent-Magnet, Brushless Machines*" IEEE, 2001.

[2] A.Cavagnino, M.Lazzari, F.Profumo, A.Tenconi, "*A Comparison Between the Axial Flux and the Radial Flux Structures for PM Synchronous Motors*" Politecnico di Torino, 2001.

[3]Jacek F. Gieras, Rong-Jie Wang, Maarten J. Kamper, "*Axial Flux Permanent Magnet Brushless Machine*" Kluwer Academic Publishers, 2004.

[4] Mickaël Kremer, "*Electromagnetic design of a disc rotor electric machine as integrated motor-generator for hybrid vehicles*" Work of thesis at Université de Haute-Alsace, 2016.

[5] Pavel Ponomarev, J. Pyrhönen, Pia Lindh, "*Effect of Slot-and-Pole Combination on the Leakage Inductance and the Performance of Tooth-Coil Permanent-Magnet Synchronous Machines* " IEEE, 2013.

[6] Pavel Ponomarev, Yulia Alexandrova, Ilya Petrov, Pia Lindh, Elena Lomonova, Juha Pyrhönen, "*Inductance Calculation of Tooth-Coil Permanent-Magnet Synchronous Machines*" IEEE, 2014.

[7] H. Shokrollahi, K. Janghorban "*Soft magnetic composite materials (SMCs)*" Journal of Materials Processing Technology, 2007.

[8] G. De Donato, F. Giulii Capponi, F. Caricchi "*Fractional-Slot Concentrated-Winding Axial-Flux Permanent Magnet Machine with Core-Wound Coils*" University of Rome "La Sapienza", 2010.

[9] Merve Yıldırım, Mehmet Polat, H. Kurum "*A survey on comparison of electric motor types and drives used for electric vehicles*" Research Gate, 2014.

[10] Werner Jara, Carlos Madariaga, Juan Tapia, Juha Pyrhönen, Pia Lindh, Javier Riedemann "*Closed-Form Solution for the Slot Leakage Inductance of Tooth-Coil-Winding Permanent Magnet Machines*" IEEE, 2018.

[11] Zhou Ye, "*Modelling and experimental analysis of core losses of SMC components*" Presented at World Congress PM2014 in Orlando USA, 2014.

[12] J. Pyrhönen, Pia Lindh, A. Parviainen, Markku Niemelä, "*Concentrated Wound PM Motors with Semi-Closed Slots and with Open Slots*" Article in International Review of Electrical Engineering, 2010.

[13] Toda Hiroaki, Wang Jiabin, Howe David, "*Analysis of Motor Loss in Permanent Magnet Brushless Motors*" JFE TECHNICAL REPORT, 2005.

[14] Michael U Lampérth, Adam C Malloy, Adrian Mlot, Mark Cordner, "*Assessment of Axial Flux Motor Technology for Hybrid Powertrain Integration*" International Electric Vehicle Symposium and Exhibition, 2015.

[15] Santiago, J., Bernhoff H., Ekergård B., Eriksson S., Ferhatovic S, "*Electrical Motor Drivelines in Commercial All Electric Vehicles: a Review*", IEEE, 2012.

[16] Juha Pyrhonen, Tapani Jokinen, Valeria Hrabovcov, "*Design of rotating electrical machines*" John Wiley & Sons, 2008.

[17] H. Shokrollahi, K. Janghorban, "*Soft magnetic composite materials (SMCs)* ", Journal of Materials Processing Technology 189 (2007) 1–12.

[18] Tanver Yazdan, Shahid Atiq, Byung-Il Kwon, Noman Baloch, Jung-Woo Kwon, "*Two Phase Dual-Stator Axial-Flux PM BLDC Motor With Ironless Rotor Using Only-Pull Drive Technique*" IEEE, 2019.